Mechanism of RanGTP priming the release of H2A-H2B from Kap114 and Importin-9

Jenny Jiou[#1], Joy M. Shaffer[#2], Natalia E. Bernades[1], Kiran Tripathi[2], Ho Yee J. Fung[1], Oladimeji S. Olaluwoye[2], Juliana Kikumoto Dias[2], Yuh Min Chook*[1], and Sheena D'Arcy*[2]

[1] Department of Pharmacology, University of Texas Southwestern Medical Center, Dallas, United States, 75390

[2] Department of Chemistry and Biochemistry, University of Texas at Dallas, Richardson, United States, 75080

[#] Co-first author

* Corresponding authors

For correspondence:

Sheena.DArcy@utdallas.edu

YuhMin.Chook@utsouthwestern.edu

Abstract:

Previously we showed that the nuclear import receptor Importin-9 wraps around the H2A-H2B core to chaperone and transport it from the cytoplasm to the nucleus (Padavannil et al. 2019). However, unlike most nuclear import systems where RanGTP dissociates cargoes from their importins, RanGTP binds stably to the Importin-9•H2A-H2B complex and formation of RanGTP•Importin-9•H2A-H2B facilitates H2A-H2B release to the assembling nucleosome (Padavannil et al. 2019). Here we show cryo-EM structures of Importin-9•RanGTP and of its yeast homolog Kap114, including Kap114•RanGTP, Kap114•H2A-H2B, and RanGTP•Kap114•H2A-H2B. In combination with hydrogen-deuterium exchange analysis of Importin-9 complexes and nucleosome assembly assays, we explain how the conserved Kap114/Importin-9 importins bind H2A-H2B and RanGTP simultaneously and how the GTPase primes histone transfer to the nucleosome. We show that RanGTP binds to the N-terminal repeats of Kap114/Importin-9 as in Kap114/Importin-9•RanGTP, and H2A-H2B binds via its acidic patch to the Kap114/Importin-9 C-terminal repeats as in Kap114/Importin-9•H2A-H2B. RanGTP-binding in RanGTP•Kap114•H2A-H2B changes Kap114/Importin-9 conformation such that it no longer contacts the surface of H2A-H2B proximal to the H2A docking domain that drives nucleosome assembly, positioning it for transfer to the assembling nucleosome. The reduced affinity of RanGTP for Kap114/Importin-9 when H2A-H2B is bound may ensure release of H2A-H2B only at chromatin.

Introduction:

In the nucleus, core histones H2A, H2B, H3 and H4 organize DNA into nucleosomes as 147 base pairs of DNA wrapped around the $(H3\text{-}H4)_2$ tetramer and two H2A-H2B dimers (Luger et al. 1997). Core histones are synthesized in the cytoplasm and folded into heterodimers that are actively transported into the nucleus by nuclear import receptors (importins) of the Karyopherin-β family. Cellular studies in *Saccharomyces cerevisiae* (*Sc*) and proteomic analysis of human cells identified the primary importins for H2A-H2B to be *Sc*Kap114 (Mosammaparast et al. 2001) and human homolog Importin-9 (Imp9, also known as IPO9) (Mühlhäusser et al. 2001; Kimura et al. 2017). It was previously also suggested that negatively-charged importins could act as chaperones for highly positively charged nucleic acid-binding proteins (such as core histones) in addition to transporting them into the nucleus (Jäkel et al. 2002). The crystal structure of Imp9 bound to H2A-H2B showed the spiral-shaped HEAT-repeat containing importin wrapping around the globular histone-fold domain of H2A-H2B (Padavannil et al. 2019). This mode of interaction occludes large surfaces on H2A-H2B that bind DNA and H3-H4 in the nucleosome (Padavannil et al. 2019). Imp9 thus acts as a histone chaperone that shields H2A-H2B from spurious interactions with nucleic acids and proteins while transporting it from the cytoplasm into the nucleus.

After the Imp9/Kap114•H2A-H2B complex is transported into the nucleus across the nuclear pore complex, H2A-H2B still needs to be delivered to assembling nucleosomes. Typically, importin-cargo complexes are dissociated by the GTP-bound Ran GTPase in the nucleus (Dirk Görlich et al. 1996; Weis 2002; Wente and Rout 2010; Soniat and Chook 2015). High concentration of RanGTP in the nucleus is maintained by Ran guanine nucleotide exchange factor, RCC1, which is chromatin-bound and catalyzes the exchange to RanGTP (Nemergut et al. 2001; Makde et al. 2010). RanGTP often binds importin and releases cargo into the nucleus (Chook and Blobel 1999; D. Görlich and Kutay 1999; Bednenko, Cingolani, and Gerace 2003; Cook et al. 2007; Wing, Fung, and Chook 2022). However, nuclear import of H2A-H2B by Imp9 seems to be an exception to this Ran-mediated cargo release mechanism. RanGTP does not release H2A-H2B from Imp9; instead, RanGTP binds the Imp9•H2A-H2B complex to form a stable RanGTP•Imp9•H2A-H2B complex (Padavannil et al. 2019). Within this ternary complex, RanGTP-binding modulates Imp9-H2A-H2B interactions to allow H2A-H2B-DNA interactions and to facilitate deposition of H2A-H2B onto an assembling nucleosome. Pemberton and colleagues also found a stable assembly containing Imp9 homolog Kap114, H2A-H2B, RanGTP and histone chaperone Nap1 in the yeast nucleus (Mosammaparast, Ewart, and Pemberton 2002).

It was unclear how Imp9/Kap114 bound H2A-H2B and RanGTP simultaneously as this ternary complex is atypical among nuclear import complexes. It was also not known how RanGTP-binding changed Imp9-H2A-H2B interactions within the ternary complex to facilitate nucleosome assembly. We solved cryo-EM structures of binary complexes Imp9•RanGTP, Kap114•RanGTP and Kap114•H2A-H2B, which collectively show conservation of H2A-H2B and RanGTP recognition by Imp9 and its yeast homolog Kap114. Comparison of the H2A-H2B- *versus* Ran-bound binary complexes showed conformational changes at the N-terminal HEAT repeats of the importins even though there are few overlaps in the importin residues that bind H2A-H2B and RanGTP. The C-terminal HEAT repeats of the importins make extensive interactions with H2A-H2B but make no contact with RanGTP and are thus flexible in the importin•Ran structures. Most importantly, we solved the structure of the RanGTP•Kap114•H2A-H2B ternary complex and used hydrogen deuterium exchange coupled to mass spectrometry to understand the dynamics of the binary and ternary complexes of Imp9. Together, the structural and solution studies show that Kap114/Imp9 binds H2A-H2B differently in the ternary complex. The Kap114/Imp9 C-terminal HEAT repeats maintain extensive contacts with the nucleosomal DNA and H3-H4-binding surfaces of H2A-H2B, but the Kap114 N-terminal HEAT repeats no longer contact the remaining nucleosomal DNA-binding surface of H2A-H2B. The exposed H2A-H2B surface allows interactions with DNA, facilitating transfer of H2A-H2B to the assembling nucleosome.

Results:

Interactions of Kap114 with H2A-H2B and RanGTP

We used pull-down binding assays, electrophoretic mobility shift assays (EMSAs), and analytical ultracentrifugation sedimentation analysis (AUC) to characterize Kap114 binding to H2A-H2B and RanGTP. In the binding assays, immobilized maltose-binding protein (MBP)-Kap114 fusion bound H2A-H2B alone, RanGTP alone, and H2A-H2B and RanGTP simultaneously, showing that RanGTP does not cause displacement of H2A-H2B from Kap114 (Figure 1A, controls in Figure 1 - Supplement 1A). EMSAs further show that Kap114 bound 1:1 with H2A-H2B or RanGTP and verified formation of a ternary complex of RanGTP•Kap114•H2A-H2B (Figure 1B, Figure 1 - Supplement 1B). This stable ternary complex sediments at 7.4 S, compared to binary Kap114•RanGTP and Kap114•H2A-H2B complexes that sediment at 6.3 S and 6.7 S respectively (Figure 1C). As a measure of histone chaperone activity of Kap114, we performed DNA competition with Kap114/Imp9 in the presence and absence of RanGTP (Figure 1D, Figure 1 - Supplement 1C, D). Both Imp9 and Kap114 bound H2A-H2B and released DNA from DNA•H2A-H2B while Imp9•RanGTP and Kap114•RanGTP did not (Figure 1D, compare lanes 4-6 and 8-10 of Figure 1 - Supplement 1D). These results are consistent with Padavannil et al. where the presence of RanGTP changes Kap114/Imp9-H2A-H2B chaperoning ability (Padavannil et al. 2019). Kap114 and Imp9 are thus similar in having histone chaperone activity, in forming a ternary complex with RanGTP and H2A-H2B, and in RanGTP modulating importin-histone interactions within the ternary complex.

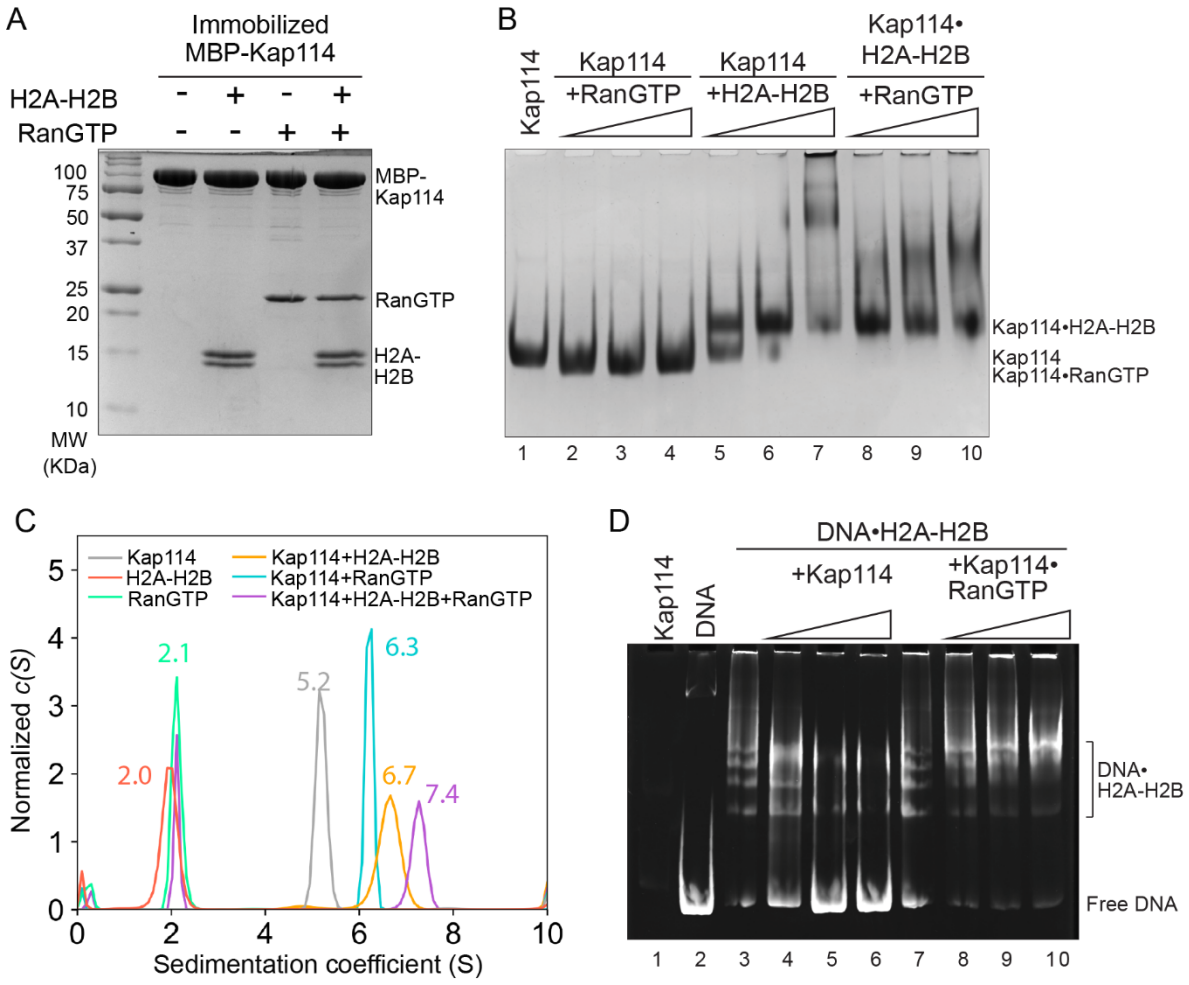

Figure 1. Kap114 binding to H2A-H2B and RanGTP. (**A**) Pull-down binding assay of MBP-Kap114 immobilized on amylose beads with H2A-H2B and RanGTP. After extensive washing, bound proteins were visualized by Coomassie-stained SDS-PAGE. Controls are shown in ***Figure 1 - Supplement 1A***. (**B**) Constant Kap114 (lanes 2-7) was titrated with 0.5, 1, or 1.5 molar ratio of RanGTP (lanes 2-4) or H2A-H2B (lane 5-7). Constant Kap114•H2A-H2B was titrated with 0.5, 1, or 1.5 molar ratio of RanGTP (lanes 8-10). Protein was visualized by Coomassie-stained native PAGE. (**C**) AUC sedimentation profiles of Kap114 (grey), H2A-H2B (red), RanGTP (green), 1:1 molar ratio of Kap114:H2A-H2B (orange), 1:1 molar ratio of Kap114:RanGTP (blue), and 1:1:3 molar ratio of Kap114:H2A-H2B:RanGTP (purple). (**D**) DNA competition assay with Kap114 (lanes 4-6) titrated at 0.5, 1, or 1.5 molar equivalents of H2A-H2B (in a DNA•H2A-H2B 1:7 complex), while Kap114•RanGTP (1:1, lanes 8-10) is titrated at 0.25, 0.5, or 1.0 molar equivalents of H2A-H2B (in a DNA•H2A-H2B 1:7 complex). Native PAGE was visualized with ethidium bromide. Coomassie staining is shown in ***Figure 1 - Supplement 1C***. Source data for A, B, and D is in ***Figure 1 - Source Data 1-3*** respectively.

Structures of binary complexes Imp9•RanGTP, Kap114•RanGTP and Kap114•H2A-H2B

We solved cryo-EM structures of the following binary complexes: Kap114•H2A-H2B (3.2 Å resolution), Kap114•RanGTP (3.5 Å resolution), and Imp9•RanGTP (3.78 Å resolution) (Figure 2A-C, Figure 2 - Supplement 1, 2, Supplement Table 1, 2). Imp9 and *Sc*Kap114 are 21.2% identical in sequence and share all key structural features, including 20 HEAT repeats (h1-h20, each containing antiparallel helices a and b) and three long loops (the h8 loop, the h18-h19 loop, and the acidic h19 loop) (Figure 2 - Supplement 4-6). Structures of Imp9 and Kap114 bound to H2A-H2B or to RanGTP are very similar.

When bound to H2A-H2B, Kap114 adopts a compact, super-helical architecture that is similar to Imp9 bound to H2A-H2B (Figure 2A, Figure 2 - Supplement 5). The Kap114 superhelix wraps around the H2A-H2B core using interactions conserved with Imp9 (Figure 2 - Supplement 5). The C-terminal ends of h3-h5 b-helices, the loops that follow these helices and helix h2b, the loops of h17 and h18 repeats, the C-terminal end of h19a helix, and the long h18-h19 loop, all contact H2A-H2B (Figure 2 - Supplement 5). Sequence comparison of Kap114 and Imp9 reveals greatest identity in the C-terminal HEAT repeats (27.3% identity aligning 319 residues of h16-h20); the h18-h19 loop is especially conserved. The N-terminal HEAT repeats (20.8% identity aligning 240 residues of h1-h5) and the central HEAT repeats (17.9% identity aligning 549 residues of h6-h15) are also conserved. This sequence conservation is consistent with similar H2A-H2B binding by Kap114 and Imp9 at both their C- and N-terminal HEAT repeats.

RanGTP-bound structures of Kap114 and Imp9 are also very similar and are like the many previously reported importin•Ran structures (Figure 2B, Figure 2 - Supplement 6) (Chook and Blobel 1999; Vetter et al. 1999; Lee et al. 2005; Grünwald and Bono 2011; Kobayashi and Matsuura 2013; Maertens et al. 2014; Tsirkone et al. 2014; Bernardes et al. 2022). Kap114 and Imp9 primarily use the b-helices of h1-h4 to bind Switch 1, Switch 2 and helix α3 of RanGTP. Other interactions involve the extended h8 loops and h12-15 of the Importins contacting helix α4 and Switch 1 of RanGTP, respectively (Figure 2 - Supplement 6). The C-terminal repeats of Kap114 (h16-h20) make no contact with RanGTP, consistent with three equally-represented classes of Kap114•RanGTP cryo-EM particles that differ in the orientations of their C-terminal repeats (Figure 2 – Supplement 2; only class 1 structure is determined and shown in Figure 2B). The flexible C-terminal repeats of Kap114 are also consistent with the lack of density for the likely very flexible h16-h20 of Imp9•RanGTP (Figure 2 – Supplement 1B).

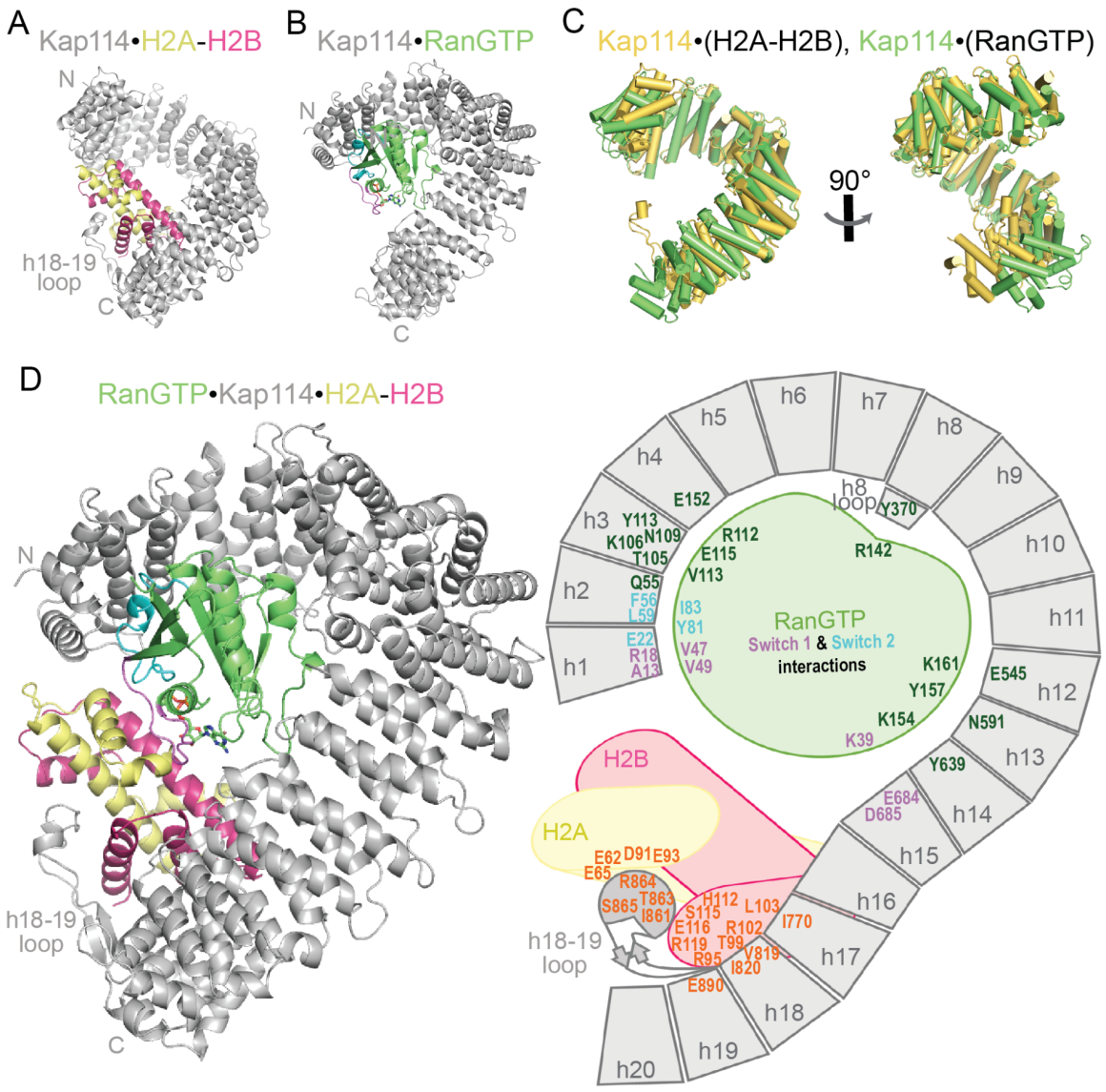

Figure 2. Cryo-EM structures of Kap114•H2A-H2B, Kap114•RanGTP and RanGTP•Kap114•H2A-H2B. (**A**) Cartoon representation of Kap114•H2A-H2B, with Kap114 in gray, H2A in yellow and H2B in red. (**B**) Cartoon representation of Kap114•RanGTP. Switch 1 (violet), Switch 2 (cyan) and GTP (sticks colored by atom) of RanGTP (green) are shown. (**C**) Superposition of Kap114 from Kap114•H2A-H2B (yellow) and Kap114•RanGTP (green) aligned at HEAT repeats h5-h13 (RMSD=0.515 Å). (**D**) Cartoon representation of RanGTP•Kap114•H2A-H2B (left) and a schematic showing interacting residues (right). H2A-H2B interactions are labeled in orange and RanGTP interactions are violet (Switch 1), cyan (Switch 2), and green.

Comparison of the Kap114•H2A-H2B and Kap114•RanGTP structures show minimal overlap between residues that contact H2A-H2B *versus* RanGTP (Figure 2 - Supplement 4). However, the importin conformations, especially at the N-terminal regions, are quite different when bound to the two ligands (Figure 2A-C). The RanGTP-bound Kap114 superhelix is wider and has a shorter pitch than the H2A-H2B-bound one (Figure 2C). HEAT repeats alignment between the Kap114•H2A-H2B and Kap114•RanGTP structures revealed rigid body regions and hinges between them that describe the conformational differences (Figure 2 - Supplement 7A). Repeats h5-h13 are similar in the two structures (RMSD=0.515 Å for 378 of 430 Cα atoms aligned), suggesting a rigid body block. Meanwhile, high RMSDs when aligning consecutive repeats suggest that h4-h5, h13-h14 and h16-h17 are hinges about which groups of HEAT repeats rotate (Figure 2 - Supplement 7A). These groups of repeats are 1) h1-h4 that contact H2A-H2B and also RanGTP, 2) the invariant h5-h13 core and 3) the h17-h20 repeats that make no contact with RanGTP and are very flexible in Kap114•RanGTP but make extensive contacts with H2A-H2B. The hinges at h4-h5 facilitate movement of the N-terminal repeats (h1-h4) relative to the central core repeats (h5-h13) while the h13-h14 and h16-h17 hinges facilitate movement of the C-terminal repeats (h17-h20) relative to the central core repeats (Figure 2C, Figure 2 - Supplement 7A). Similar features of conformational change are observed for Imp9•H2A-H2B and Imp9•RanGTP (Figure 2 - Supplement 7B).

Structure of the RanGTP•Kap114•H2A-H2B ternary complex

It was unclear from the binary structures how the ternary complex is arranged when Kap114 binds RanGTP and H2A-H2B simultaneously. We assembled the RanGTP•Kap114•H2A-H2B complex for structure determination by cryo-EM. The data collected produced three classes of ternary complexes that differ in the orientations of Kap114 repeats h16-h20. We solved the structure of the most highly populated class 3 (Figure 2D, Figure 2 - Supplement 3, Figure 3 - Supplement 1A). The structure of this most open/fanned-out conformation of the RanGTP•Kap114•H2A-H2B complex was determined to 3.3 Å resolution (Figure 2D, Figure 2 - Supplement 3, Table 1).

The RanGTP•Kap114•H2A-H2B structure (Figure 2D) shows the N-terminal half of Kap114 superhelix (composed of h1-h15) binding RanGTP by adopting the same conformation (RMSD=0.625 Å, 587 of 701 Cα atoms aligned) and making the same interactions with the GTPase as the binary Kap114•RanGTP structure (Figure 3A, B, Figure 3 - Supplement 2). Most of the residues in the Kap114 h1-h4 repeats that contact H2A-H2B in Kap114•H2A-H2B are still accessible but not in the same conformation and thus no longer contact the histone in the ternary

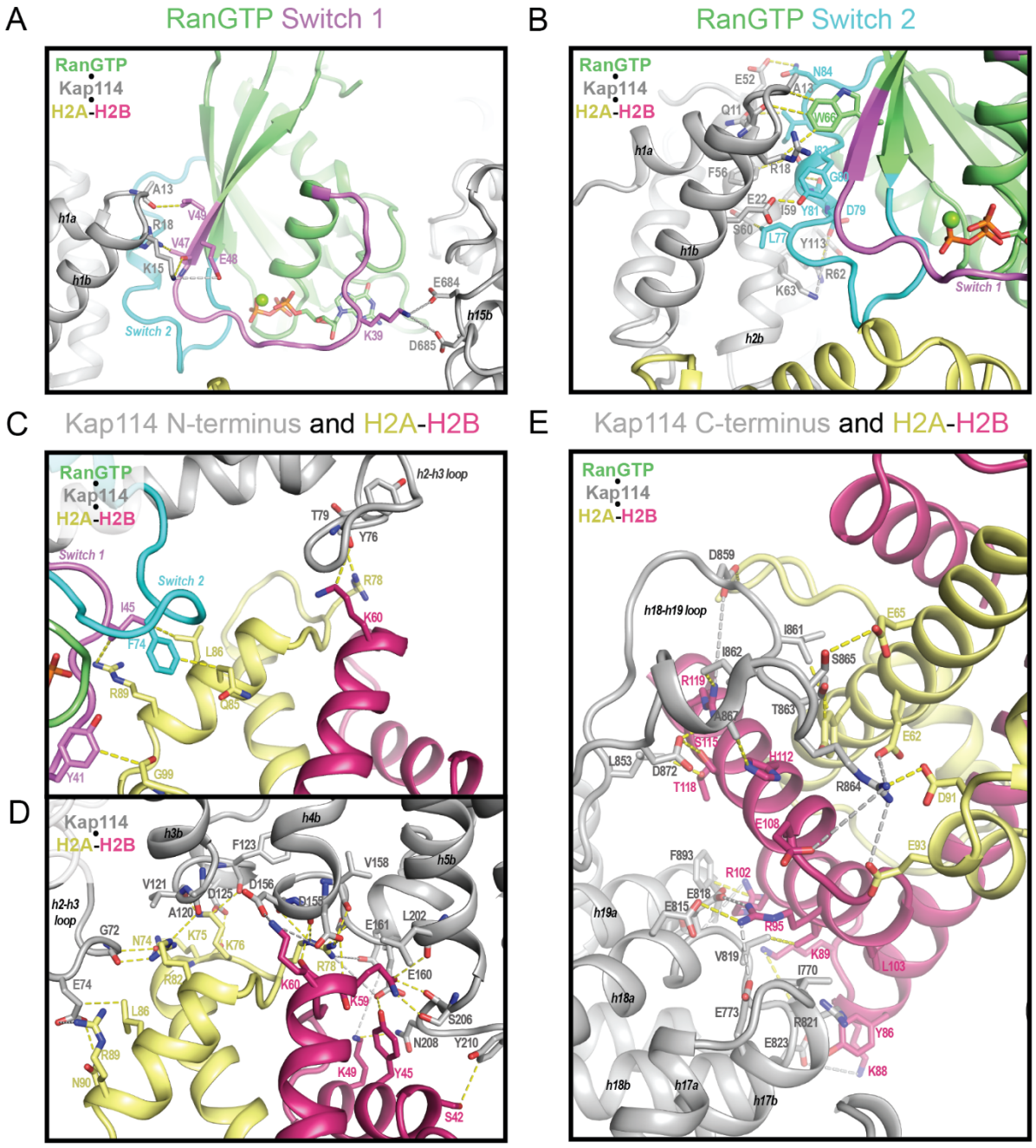

Figure 3. Interactions of the ternary RanGTP•Kap114•H2A-H2B complex at (**A**) RanGTP Switch 1 (**B**) RanGTP Switch 2, (**C**) N-terminal repeats and (**D**) C-terminal repeats of Kap114. (**E**) The N-terminal repeats of Kap114 in the binary Kap114•H2A-H2B complex for comparison with (**C**). In all panels, Kap114 is gray, RanGTP is green with Switch 1 in violet and Switch 2 in cyan, H2A is yellow, and H2B is red. Dashed lines represent interactions <4 Å (yellow) and long-range electrostatic interactions <8 Å (gray).

structure (Figure 3C, D). This 'displaced' surface of H2A-H2B makes a few contacts with the Kap114 h2-h3 loop and the RanGTP switches, a drastic decrease in interaction when compared to Kap114•H2A-H2B (Figure 3C, D). This newly exposed surface of H2A-H2B is also proximal to the H2A C-terminal tail that docks onto H3-H4 in the nucleosome, although this tail is not visible in either structure.

The region C-terminal of h16 in Kap114 does not contact RanGTP but adopts the same conformation and maintains the same extensive contacts with H2A-H2B as in the Kap114/Imp9•H2A-H2B structures (Figure 3E, Figure 3 - Supplement 3). The C-terminal region of Kap114, with H2A-H2B bound, adopts different orientations relative to the N-terminal half of the importin in the different cryo-EM classes of particles (Figure 2D, Figure 2 - Supplement 3, Figure 3 - Supplement 1). The movements of the histone-bound Kap114 C-terminal region likely occur about the hinge at h16-h17.

Solution analysis of Imp9•H2A-H2B and Imp9•RanGTP binary complexes

To probe Imp9/Kap114 complexes in solution, we performed bottom-up HDX-MS focusing on Imp9 for which a ternary complex structure is not available (Figure 4-7, Figure 4 - Supplement Tables 3-6). Comparison of D-uptake between binary complexes and Imp9 alone clearly identifies known interfaces in Imp9•H2A-H2B and Imp9•RanGTP (Figure 4A-D, 5A Panels 1-2, 6A Panels 1-2, Figure 4 - Supplement 1A Panels 1-2). Upon addition of H2A-H2B, reduced D-uptake occurred within the Imp9 N-terminal repeats at the h4-h5 loop, h5, and, to a lesser extent, h6 (Figure 4A, B, 5A Panel 1). It also occurred within the C-terminal repeats at the h18 loop, the start and end of the h18-h19 loop, and the C-terminal end of the h19 a-helix (Figure 4B, 6A Panel 1). These regions correspond to the binding sites of H2A-H2B in Imp9 (Padavannil et al. 2019).

Addition of RanGTP similarly reduced D-uptake within the Imp9 N-terminal repeats at h1 and the h3 loop, as well as within the middle repeats at the h8 loop and h13 repeat (Figure 4C, D, 5A Panel 2, Figure 4 – Supplement 1A Panel 2). These are the regions used by Imp9 in the structure to bind RanGTP (Figure 2 - Supplement 6). Beyond known interfaces, we also see reduced D-uptake with either H2A-H2B or RanGTP in the Imp9 h8 loop, h16-h17 repeats and the flexible/disordered h19 loop (Figure 4B, D, 5A Panels 1-2, 6A Panels 1-2, Figure 4 – Supplement 1A Panels 1-2). The larger reduction in D-uptake for h16-h17 with H2A-H2B than RanGTP is notable as it is likely a hinge that positions the C-terminal repeats for histone-binding.

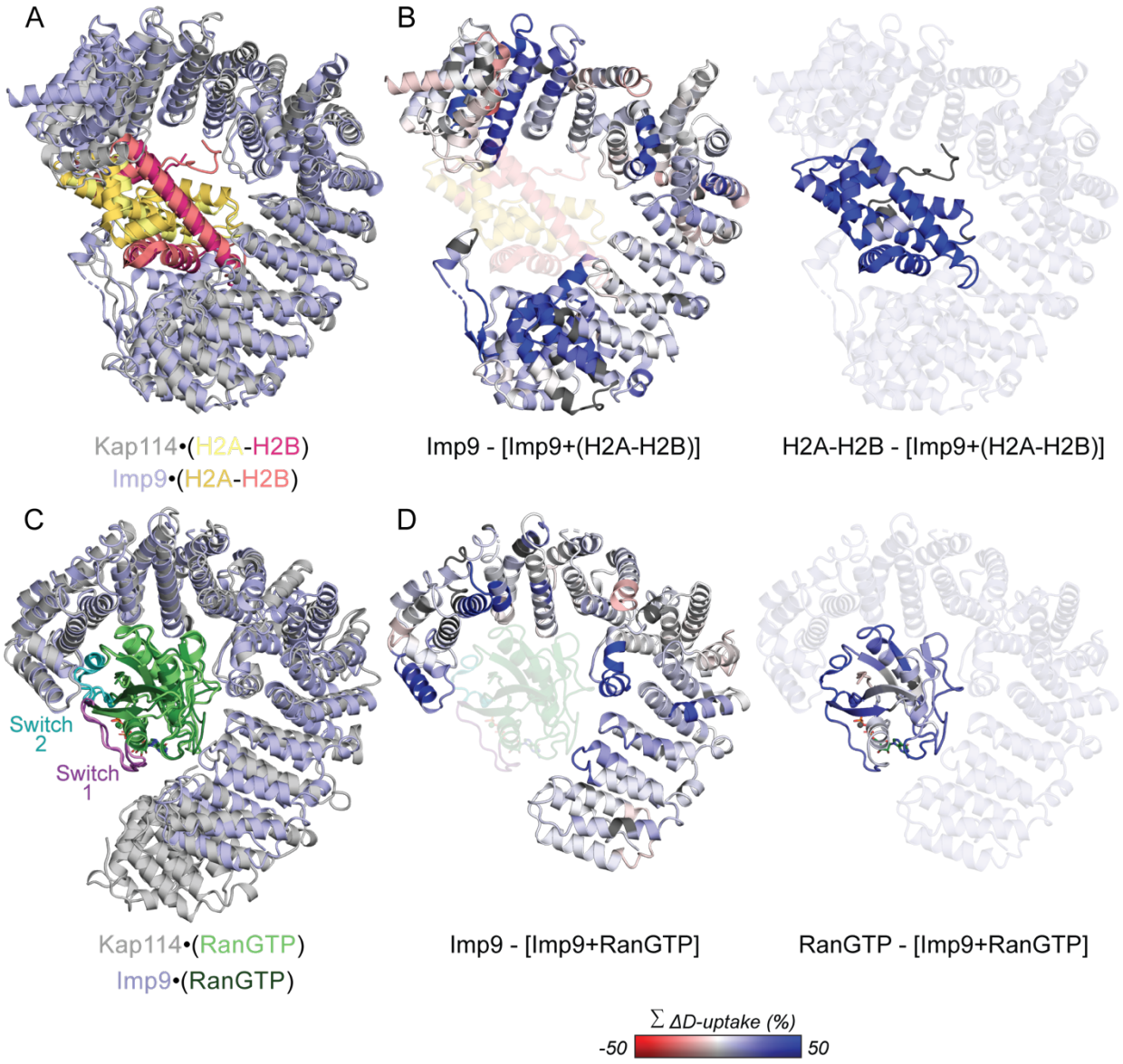

Figure 4. Hydrogen-deuterium exchange of binary Imp9 complexes. (**A**) Superposition of Imp9 (blue) and Kap114 (gray) bound by H2A-H2B (yellow-pink) (RMSD=4.848 Å). (**B**) Imp9 (left) or H2A-H2B (right) colored according to the change in D-uptake percent upon binary complex formation summed across all timepoints (∑ ΔD-uptake). (**C**) Superposition of Imp9 (blue) and Kap114 (gray) bound by RanGTP (green with Switch 1 purple and Switch 2 cyan) (RMSD=4.114 Å). (**D**) Imp9 (left) or RanGTP (right) colored according to the change in D-uptake percent upon binary complex formation summed across all timepoints (∑ ΔD-uptake). For (B) and (D), the scale is -50 to 50% (red to blue) and is based on DynamX residue-level scripts without statistical filtering. Residues without coverage are dark gray.

We can also compare D-uptake of peptides from RanGTP or H2A-H2B alone to those in the binary complexes (Figure 4B, D, Figure 7A Panel 1, Figure 4 – Supplement 2). For RanGTP, the greatest reduction in D-uptake upon addition of Imp9 occurred at Switch 1, followed by Switch 2, residues 93-120 (near Imp9 h3 loop), and residues 121-158 (near Imp9 loops of h7, h8, h13 and h14), all aligning with interfaces seen in the Imp9•RanGTP structure (Figure 4D, Figure 2 - Supplement 6). For H2A-H2B, however, we observed reduced D-uptake upon addition of Imp9 throughout the entire H2A and H2B histone-fold domains, as well as the H2B C-terminal helix (Figure 4B, Figure 4 - Supplement 2). This widespread effect of Imp9 parallels other histone chaperones that globally stabilize the folded regions of H2A-H2B (Liu et al. 2020). We do not have coverage of the N-terminal tails of H2A or H2B, and consistent with the Imp9•H2A-H2B structure where the H2A C-terminal tail remains disordered, we see maximum deuteration of the C-terminal tail of H2A in both H2A-H2B alone and Imp9•H2A-H2B (Figure 4B, Figure 4 - Supplement 2A, B).

Solution analysis of the RanGTP•Imp9•H2A-H2B ternary complex

Solution analysis of the Imp9 ternary complex also suggests an arrangement similar to that seen in the RanGTP•Kap114•H2A-H2B structure. Comparison of Imp9 with H2A-H2B and Imp9 with both RanGTP and H2A-H2B, showed that addition of RanGTP caused an increase in D-uptake in h4-h5, indicative of less H2A-H2B occupancy at the Imp9 N-terminal repeats (Figure 5A Panels 3-4, B, C). Unlike the N-terminal repeats, addition of RanGTP did not alter D-uptake of the h18 loop or the start of the h18-19 loop, showing that H2A-H2B maintains binding at these C-terminal repeats in the presence of RanGTP (Figure 6A Panels 3-4, B, C). We do, however, observe less D-uptake at the h19 a-helix and in the h19 loop, suggesting subtly weaker contacts at this point. The ternary complex also has less D-uptake at the h16-h17 hinge, consistent with RanGTP causing a rigid body movement of the C-terminal repeats similar to that seen in the Imp9•RanGTP (Figure 6A, B, Figure 6 - Supplement 1). Changes in H2A-H2B D-uptake also occurred, albeit with smaller magnitude that for many peptides was just below our stringent significance cutoffs (Figure 4 - Supplement 2). Binding of RanGTP caused increased D-uptake of H2A α1 suggesting increased flexibility of the H2A C-terminal tail, while decreased D-uptake occurred in H2A and H2B close to the acidic patch that is bound by the Imp9 h18-h19 loop.

The presence of H2A-H2B also reduces the occupancy of RanGTP on Imp9, an observation not predicted by the Kap114 ternary structure. This is indicated by the reduction in D-uptake upon addition of RanGTP to Imp9 being greater in the binary than in the ternary (Figure 5A Panels 2-3). This trend is seen at the RanGTP-binding site in h1-h3 (Figure 5A, B). An identical trend is observed for the RanGTP peptides involved in binding Imp9, with less change in D-uptake

occurring at Switch 1, Switch 2, and residues 93-120 and 121-158 (Figure 7A, B). Importantly, it is only the occupancy of RanGTP that is altered and not the actual contacts as the pattern of D-uptake remains the same between the binary and ternary complexes for both Imp9 and RanGTP peptides (Figure 5A Panels 2-3, 7A). Based on the reduced change in D-uptake of peptides at the RanGTP-Imp9 interface, we can estimate an affinity of ~200 nM, which is greater than the reported single digit nanomolar affinities for several Importin and RanGTP pairs (Figure 7 - Supplement Table 7) (Hahn and Schlenstedt 2011; Kochert et al. 2018). To test this prediction, we used fluorescence polarization to measure the affinity of RanGTP for Kap114/Imp9 and Kap114/Imp9•H2A-H2B (Figure 7C, D). We measure the affinities to be 0.8/1 nM and 270/150 nM, respectively (Figure 7C, D). These clearly show that the presence of H2A-H2B compromises the affinity of RanGTP to Imp9/Kap114 150- to 330-fold.

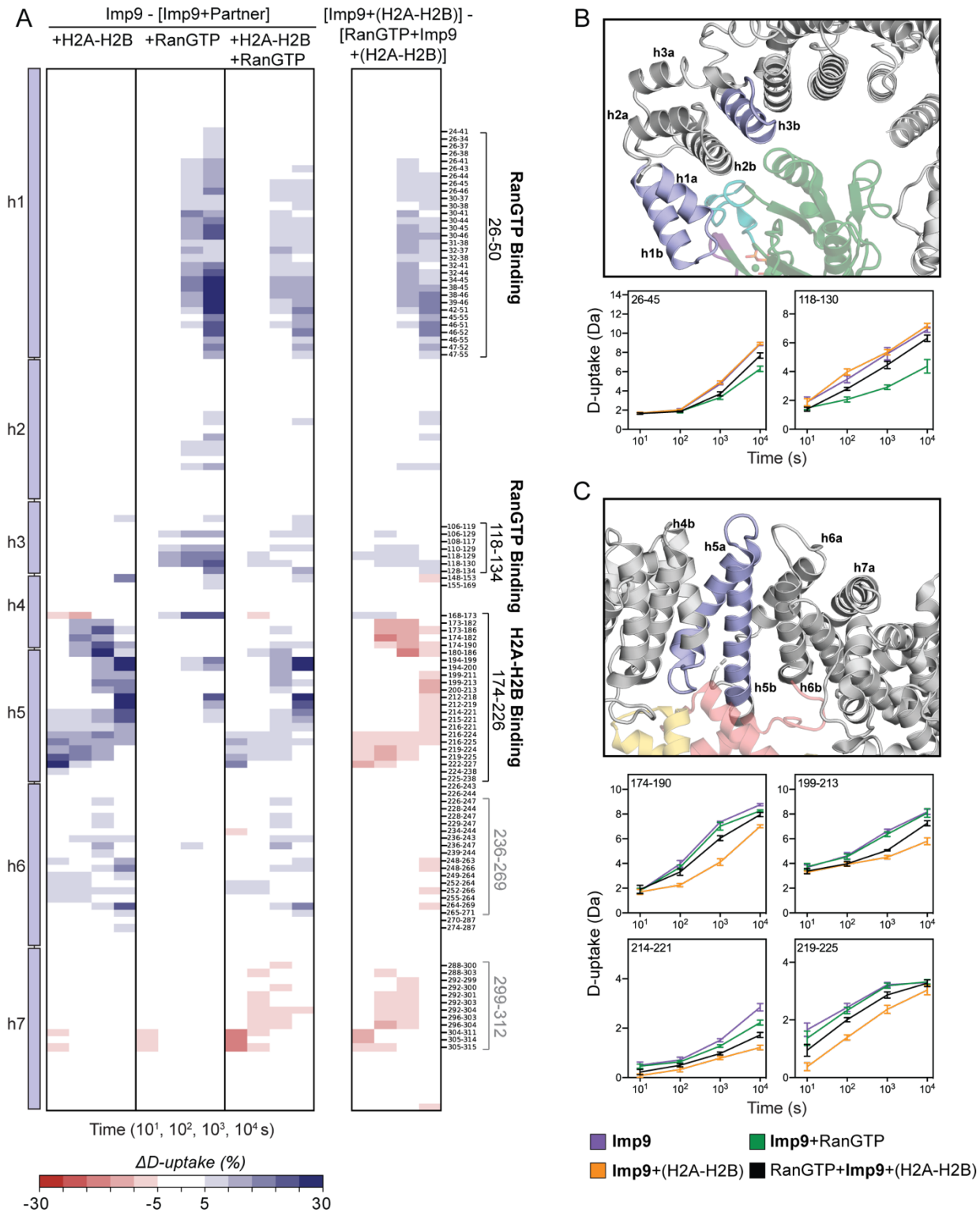

Figure 5. Fractional D-uptake differences in the N-terminal HEAT repeats of Imp9. (**A**) Differences in D-uptake between Imp9 alone and Imp9+H2A-H2B, Imp9+RanGTP, or RanGTP+Imp9+H2A-H2B in **Panels 1**, **2**, and **3**, respectively. Difference in D-uptake between Imp9+H2A-H2B and RanGTP+Imp9+H2A-H2B

is shown in **Panel 4**. Boundaries and peptides from binding sites (black) and regions of conformational change (gray) are noted. Blue/Red coloring indicates a difference ≥5% with a *p*-value ≤0.01 in a Welch's t-test (n=3). (**B**) Interface between the N-terminal HEAT repeats of Imp9 and RanGTP with example D-uptake plots for Imp9 residues 26-50 and 118-134 (colored blue on structure). (**C**) Interface between the N-terminal HEAT repeats of Imp9 and H2A-H2B with example D-uptake plots for Imp9 residues 174-226 (colored blue on structure). For B and C, D-uptake plots show Imp9 alone (purple), Imp9+H2A-H2B (orange), Imp9+RanGTP (green), and RanGTP+Imp9+H2A-H2B (black). Error bars are ±2SD with n=3. The y-axis is 80% of the maximum theoretical D-uptake, assuming complete back exchange of the N-terminal residue.

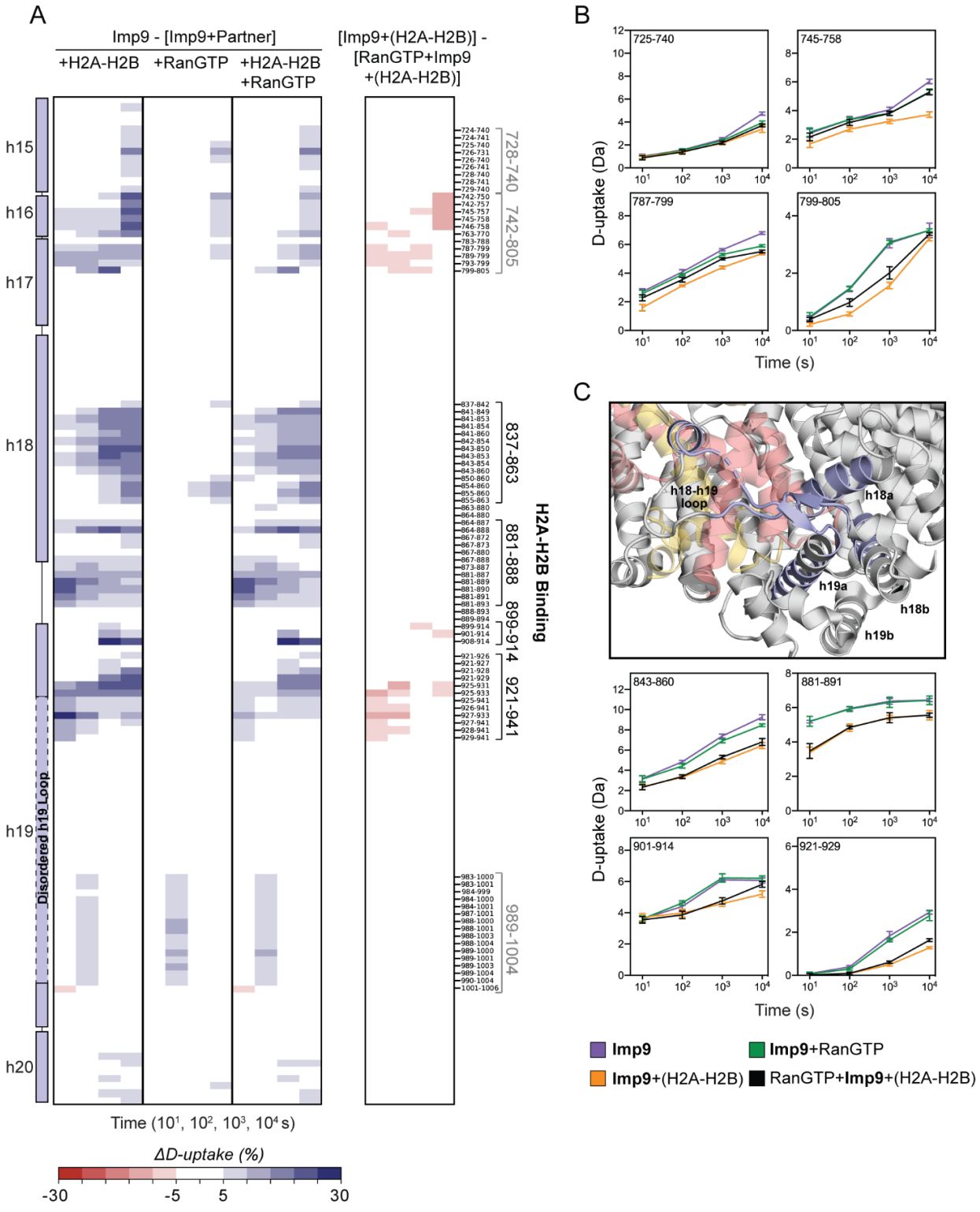

Figure 6. Fractional D-uptake differences in the C-terminal HEAT repeats of Imp9. (**A**) Difference in D-uptake between Imp9 and Imp9+H2A-H2B, Imp9+RanGTP, or RanGTP+Imp9+H2A-H2B in **Panel 1**, **2**, and **3**, respectively. Difference in D-uptake between Imp9+H2A-H2B and RanGTP+Imp9+H2A-H2B shown in

Panel 4. Boundaries and peptides from binding sites (black) and regions of conformational change (gray) are noted. Blue/Red coloring indicates a difference ≥5% with a p-value ≤0.01 in a Welch's t-test (n=3). (**B**) Region of conformational change in the C-terminal HEAT repeats of Imp9 upon binding H2A-H2B and/or RanGTP with example D-uptake plots for Imp9 residues 728-805. (**C**) Interface between the C-terminal HEAT repeats of Imp9 and H2A-H2B with example D-uptake plots for Imp9 residues 837-863, 881-888, 899-914, and 921-941 (colored blue on structure). For B and C, D-uptake plots show Imp9 alone (purple), Imp9+H2A-H2B (orange), Imp9+RanGTP (green), and RanGTP+Imp9+H2A-H2B (black). Error bars are ±2SD with n=3. The y-axis is 80% of the maximum theoretical D-uptake, assuming complete back exchange of the N-terminal residue.

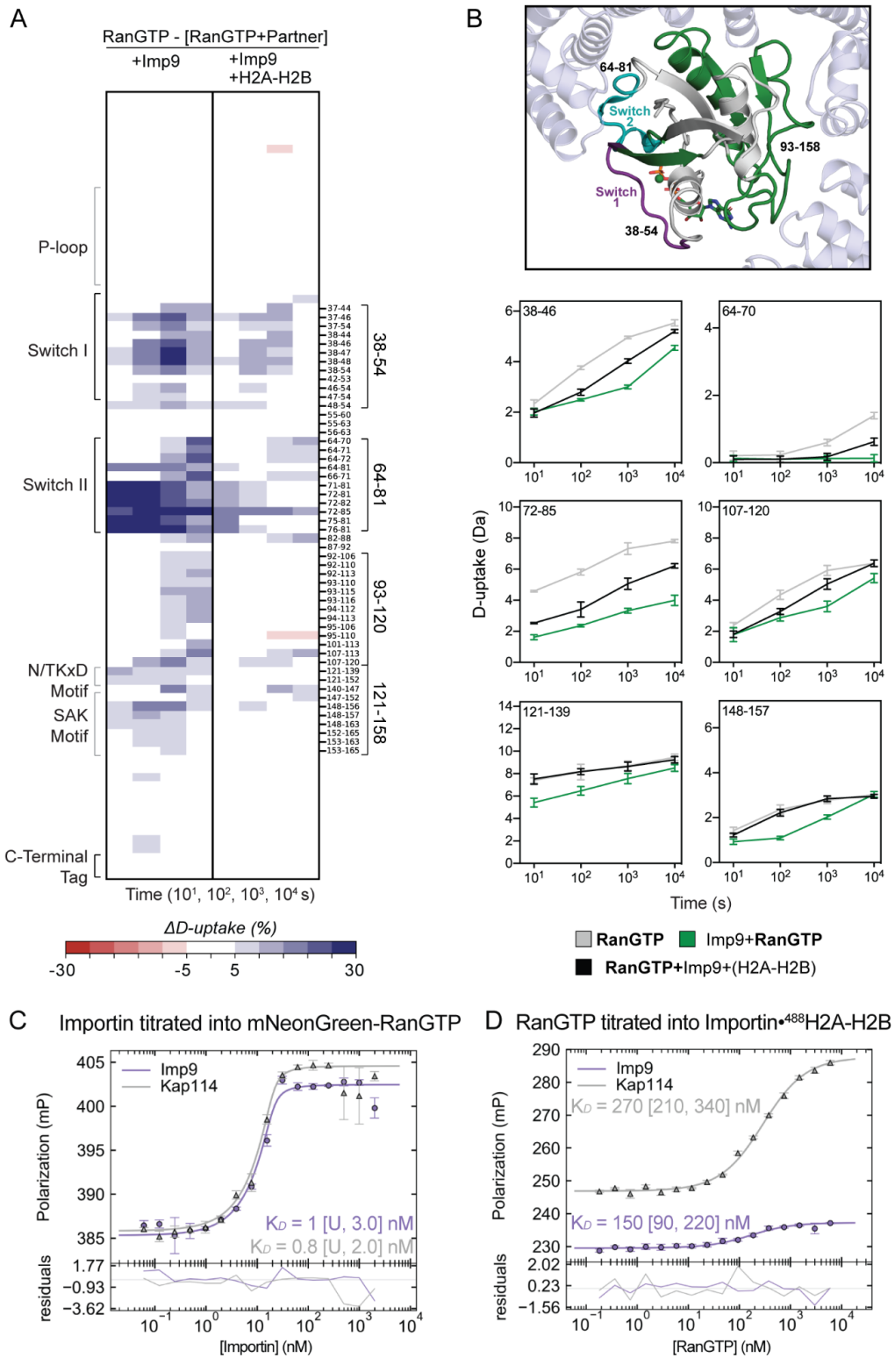

Figure 7. Fractional D-uptake differences in RanGTP. (**A**) Differences in D-uptake between RanGTP alone and Imp9+RanGTP or RanGTP+Imp9+H2A-H2B in **Panels 1**, **2**, respectively. Boundaries and

peptides from binding sites (black) are noted. Blue/Red coloring indicates a difference ≥5% with a *p*-value ≤0.01 in a Welch's t-test (n=3).(**B**) Interface between RanGTP and Imp9 with example D-uptake plots for RanGTP residues 38-54, 64-81, 93-120, and 121-158 (colored green on structure). D-uptake plots show RanGTP alone (gray), Imp9•RanGTP (green), and RanGTP•Imp9•H2A-H2B (black). Error bars are ±2SD with n=3. The y-axis is 80% of the maximum theoretical D-uptake, assuming complete back exchange of the N-terminal residue. (**C**, **D**) Affinity of RanGTP for Kap114/Imp9 and Kap114/Imp9•H2A-H2B complexes measured with fluorescence polarization. Kap114 experiments are plotted in gray, and Imp9 experiments are plotted in purple. (**C**) Kap114/Imp9 titrated into mNeonGreen-RanGTP. (**D**) RanGTP is titrated into Kap114/Imp9•^{488}H2A-H2B. ^{488}H2A-H2B contains H2A-K119C labeled with XFD488. The points in the upper plots are the mean of the triplicate measurements and the error bars are ±1SD. The residual plots below show the deviation of the mean from the fitted line.

The GTPase in RanGTP•Kap114•H2A-H2B primes transfer of H2A-H2B to nucleosome

We performed nucleosome assembly assays where we titrated H2A-H2B and Kap114 in the presence or absence of RanGTP into tetrasomes (Figure 8A, Figure 8 - Supplement 1A). Like Imp9, Kap114 facilitated H2A-H2B deposition, forming a nucleosome, only in the presence of RanGTP (Figure 8A, Figure 8 - Supplement 1A, B). Without RanGTP, Kap114/Imp9 inhibited H2A-H2B deposition. The RanGTP-induced release of the contacts between H2A-H2B and the N-terminal HEAT repeats of Kap114/Imp9 clearly makes H2A-H2B more available to form nucleosomal interactions with DNA and H3-H4. These results are consistent with our structural and solution data.

We compared the location of nucleosomal interfaces of H2A-H2B to Kap114•H2A-H2B and RanGTP•Kap114•H2A-H2B structures to understand how RanGTP facilitates H2A-H2B release to the assembling nucleosome (Figure 8B-D). In Kap114•H2A-H2B, a large portion of the nucleosomal DNA-binding surface of H2A-H2B is obstructed by the N- and C-terminal regions of Kap114 (Figures 8B, C). The region of H2A-H2B that interfaces with H3-H4 through a four-helix bundle in the nucleosomes is also covered by the C-terminal region of Kap114 (Figures 8B, C). This extensive occlusion in the binary Kap114/Imp9•H2A-H2B complex explains the poor ability to release H2A-H2B to DNA (Figure 1D) or tetrasomes (Figure 8A, Figure 8 - Supplement 1A, B). Occlusion of H2A-H2B is altered in the ternary RanGTP•Kap114•H2A-H2B structure. Although the Kap114 C-terminal repeats still cover part of the nucleosomal DNA and H3-H4-binding surfaces of H2A-H2B, the Kap114 N-terminal repeats no longer engage the remaining nucleosomal DNA-binding surface of H2A-H2B. This exposure of a long stretch of DNA-binding residues proximal to the H2A C-terminal tail, make H2A-H2B more available for potential capture by DNA (Figure 1D) or the assembling nucleosome (Figures 8B, D). These structural observations are consistent with the nucleosome assembly assays where the RanGTP•Kap114/Imp9•H2A-H2B complex effectively deposits H2A-H2B onto assembling nucleosomes (Figure 8A, Figure 8 - Supplement 1A, B).

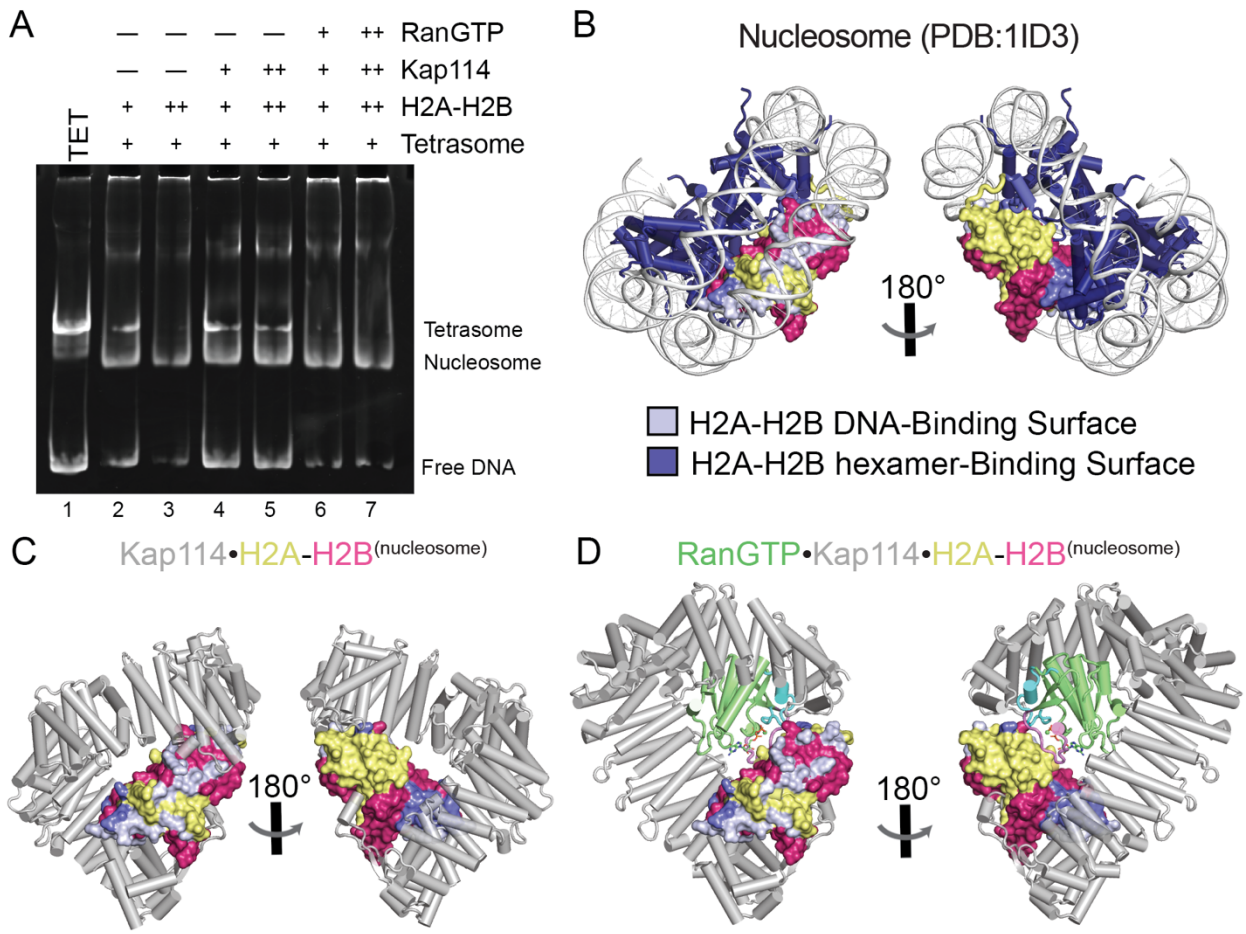

Figure 8. Nucleosome assembly assay and surface representation of nucleosomal binding surfaces on H2A-H2B. **(A)** Nucleosome assembly assay where either H2A-H2B, Kap114•H2A-H2B or RanGTP•Kap114•H2A-H2B is titrated in molar equivalents of 2.0 and 3.0 to tetrasome (TET; 1.25 μM). Ethidium bromide-stained gel is shown. The same gel is Coomassie-stained in ***Figure 8 - Supplement 1A***. Source data is in ***Figure 8 - Source Data 1***. **(B)** Nucleosome (PDB 1ID3) highlighting a single copy of H2A-H2B (yellow and red, respectively) and its interactions. One H2A-H2B core is shown as surface while the H2A C-terminal tail is shown as cartoon (as it is not visible in the importin structures). The DNA is white with its interactions on H2A-H2B colored blue-white. The histone hexamer, H2A-H2B+$(H3\text{-}H4)_2$, is navy with its interaction on H2A-H2B colored slate-blue. The surface of the nucleosome H2A-H2B core and its interaction colors are aligned and docked into (**C**) Kap114•H2A-H2B and (**D**) RanGTP•Kap114•H2A-H2B. Left and right views are 180° rotations.

Discussion:

Kap114 behaves like Imp9 in all our structural, biophysical and biochemical analyses. Their structures bound to H2A-H2B or RanGTP are very similar with only minor differences, such as no interaction between Kap114 and the H2B N-terminal tail compared to 3-5 tail residues seen bound to Imp9 (Padavannil et al. 2019).The lack of H2B tail contacts with Kap114 is consistent with previous findings that the histone tails are not important for Imp9 binding, and that the removal of the histone tails does not affect their nuclear import (Thiriet and Hayes 2001; Padavannil et al. 2019). Both Imp9 and Kap114 occlude the nucleosomal DNA-binding regions of H2A-H2B with their N-terminal HEAT repeats, and the nucleosomal histone and DNA-binding sites with their C-terminal HEAT repeats. Such extensive interfaces render Imp9 and Kap114 effective H2A-H2B chaperones that compete interactions between H2A-H2B and DNA.

However, the extensive importin-histone interactions make it difficult to release H2A-H2B in the nucleus. The mechanism of RanGTP-mediated H2A-H2B release in the nucleus is indeed unusual. Unlike other import cargos that are easily dissociated from their importins by RanGTP, the GTPase cannot release H2A-H2B from Kap114 or Imp9 (Mosammaparast, del Rosario, and Pemberton 2005; J. Baumhardt and Chook 2018; Padavannil et al. 2019). Instead, RanGTP binds to form a stable RanGTP•Kap114/Imp9•H2A-H2B complex. This ternary complex suggests that H2A-H2B may continue to be chaperoned by its importin in the nucleoplasm, in line with the generally accepted notion that there is almost no free H2A-H2B in the cell (Gunjan, Paik, and Verreault 2006; Hammond et al. 2017). Importantly, neither Kap114 nor Imp9 alone can deposit H2A-H2B onto an assembling nucleosome, and in fact they are effective competitors of histone-DNA interactions. The binding of RanGTP however causes a switch where now they release H2A-H2B to DNA and assemble nucleosomes. The stable RanGTP•Kap114/Imp9•H2A-H2B complex is thus key for H2A-H2B release in the nucleus. We showed that conformational changes in the ternary RanGTP•Kap114•H2A-H2B complex, validated by solution HDX analysis of RanGTP•Imp9•H2A-H2B, released contacts between H2A-H2B and the N-terminal HEAT repeats of the importins to make H2A-H2B available for nucleosomal interactions with DNA and H3-H4.

Although we have a cryo-EM structure of RanGTP•Kap114•H2A-H2B and it is clear how RanGTP confers accessibility or exposure of H2A-H2B for nucleosomal interactions, it is unclear if/how RanGTP might bind differently when it first encounters the binary Kap114/Imp9•H2A-H2B complex. The conformations of histone- *versus* Ran-bound importins are different, but there is almost no overlap in the importin residues that bind the two ligands. Most of the importin residues that contact RanGTP are accessible in Kap114/Imp9•H2A-H2B and perhaps some of them may

engage the GTPase weakly in an initial encounter complex even when H2A-H2B is fully engaged with both the N- and C-terminal repeats of Kap114/Imp9 (Padavannil et al. 2019). Importin fluctuations that sample multiple super-helical conformations may then result in a more stable RanGTP-bound conformation that resembles the binary Kap114/Imp9•RanGTP structures with H2A-H2B released from the N-terminal importin repeats and engaged only with the C-terminal repeats. Alternatively, there may be no separate encounter complex. Kap114/Imp9 in the binary histone complex may sample many conformations and RanGTP may selectively bind and stabilize the conformation seen in the Kap114/Imp9•RanGTP structures. The need for importin conformational change in Kap114/Imp9•H2A-H2B to bind RanGTP is consistent with the >200-fold decrease in affinity for RanGTP binding to Kap114/Imp9•H2A-H2B compared to Kap114/Imp9 alone. The decreased RanGTP affinity may be useful to limit RanGTP-binding and H2A-H2B release to locations with the highest RanGTP concentration such as at chromatin near RCC1(Nemergut et al. 2001; Fried and Kutay 2003; Weis 2003).

Although we have revealed how RanGTP primes the release of H2A-H2B from Kap114/Imp9, many questions remain about this process in cells and about Kap114/Imp9 functions in the nucleus. It is unclear if there are additional factors in the nucleus that further modulate H2A-H2B release. Kap114 was reported to be sumoylated and the modification improves the ability of RanGTP to release cargoes Sua7 (also known as TFIIb) and TBP (Rothenbusch et al. 2012). The sumoylation site, mapped to residue K909, is located in the long acidic h19 loop that is disordered in all our Kap114 structures (h19 loop deletion in Imp9 does not decrease H2A-H2B affinity;(Padavannil et al. 2019). Sumoylation may regulate RanGTP-mediated release of H2A-H2B from Kap114/Imp9 by means of intranuclear targeting. While H2A-H2B may be released directly to the assembling nucleosome, it could also be released to another H2A-H2B chaperone. Candidate chaperones include Nap1, FACT, or APLF (Chen et al. 2016; Liu et al. 2020; Corbeski et al. 2022).

It is possible that Kap114/Imp9 has roles in the nucleus in addition to H2A-H2B import and deposition into nucleosomes. Afterall, it can chaperone H2A-H2B in the nucleus when bound to RanGTP. We clearly showed that Kap114/Imp9•RanGTP cannot disassemble H2A-H2B from a nucleosome, however, it is not known if nuclear Kap114/Imp9, in the presence of RanGTP, may chaperone H2A-H2B after it is removed from the nucleosome by remodelers during replication, transcription or DNA repair (Avvakumov, Nourani, and Côté 2011; Keck and Pemberton 2012). Furthermore, the importin-histone interface in RanGTP•Kap114/Imp9•H2A-H2B involves the H2A-H2B acidic patch, which also mediates inter-nucleosome contacts that are important for

higher order chromatin structures (Luger et al. 1997; Kalashnikova et al. 2013). Kap114/Imp9 may have potential roles in modulating higher-order chromatin structure and function.

We have revealed how Kap114/Imp9 chaperones H2A-H2B in the cytoplasm, through the nuclear pore complex, and likely continues to do so in the nucleus in the form of the RanGTP•Kap114/Imp9•H2A-H2B complex. This knowledge is the foundation to understand how additional molecular players contribute to cytoplasmic H2A-H2B processing, nuclear import, and H2A-H2B deposition into the nucleosome. Studies by Pemberton and colleagues showed Kap114 associating with histone chaperone Nap1, which binds H2A-H2B in both the cytoplasm and the nucleus (Straube, Blackwell, and Pemberton 2010). Imp9 also co-purified with Nap1L1 and Nap1L4 in mammalian cells (Havugimana et al. 2012; Obri et al. 2014; Jiang et al. 2017; Woodley and Collins 2019). The Nap1-binding site of H2A-H2B overlaps with the N-terminal Kap114/Imp9-binding site, but not the C-terminal binding site (D'Arcy et al. 2013; Aguilar-Gurrieri et al. 2016; Huang, Dai, and Zhou 2020). This mode of Nap1-histone interaction may allow easy transfer of H2A-H2B from Nap1 to the Kap114 C-terminal repeats or allow both Nap1 and Kap114 to co-chaperone H2A-H2B in the cytoplasm for nuclear import. The reverse may be possible in the nucleus. The Nap1-binding site of H2A-H2B is accessible in RanGTP•Kap114•H2A-H2B for transfer of the histone to Nap1, or for Nap1 to co-chaperone the histone in a larger RanGTP•Kap114•H2A-H2B•Nap1 assembly. These scenarios are useful to guide future studies of histone biosynthesis in the cytoplasm and nucleosome assembly/disassembly in the nucleus as they resemble multiple known examples of cascades of histone co-chaperoning or transfer between histone chaperones (Elsässer and D'Arcy 2012; Dabin and Polo 2017; Pardal, Fernandes-Duarte, and Bowman 2019; Bernardes et al. 2022).

Methods:

Constructs, Protein Expression and Purification

*Sc*Kap114 was cloned into two modified vectors: pGEX-4T3 (GE Healthcare) and pmalE (New England BioLabs). The pGEX-43T was modified to have a TEV cleavage site inserted between the GST tag and Kap114. The pmalE was modified to have a His-tag at the N-terminus of MBP and a TEV cleavage site after the MBP.

The plasmid was transformed into BL21-Gold(DE3) and plated on Luria Broth (LB) agar with ampicillin for selection. Kap114 was expressed using 6 L of LB media and induced with 0.5 mM isopropyl β-D-1-thiogalactopyranoside (IPTG) for 16 h at 20°C. Cells were spun at 4,000 rpm with a Sorvall BP8 (Thermo Fisher) for 30 min at 4°C and resuspended in lysis buffer (20 mM Tris-HCl pH 7.5, 1 M NaCl, 15% (v/v) glycerol, 2 mM dithiothreitol (DTT for GST-Kap114) or 2 mM β-mercaptoethanol (BME for His_6MBP-Kap114), cOmplete EDTA-free Protease Inhibitor Cocktail (Roche Applied Science). Cells were lysed with an Emulsiflex-C5 cell homogenizer (Avestin) and centrifuged in an Avanti J-26 XPI with a JA-25.50 rotor (Beckman Coulter) at 20,000 RCF for 1 h at 4°C. The supernatant was decanted into a gravity, affinity column. GST-Kap114 was purified with Glutathione Sepharose 4B (GE Healthcare) and the GST tag was cleaved on column using TEV protease. His_6MBP-Kap114 was purified with Ni^{2+}-NTA Agarose (Qiagen). Once eluted, the Kap114 or His_6MBP-Kap114 was further purified by ion-exchange chromatography using HiTrap Q HP (GE Healthcare), and gel filtration chromatography using Superdex 200 16/600 (GE Healthcare). Proteins were stored in the gel filtration buffer containing 20 mM Tris-HCl pH 7.5, 150 mM NaCl, 2 mM DTT.

Human Imp9 and *Sc*Ran (Gsp1 residues 1-179 with Q71L) were expressed and purified as described in Padavannil et al, 2019 (Padavannil et al. 2019). *Sc*/*Xenopus laevis* (*Xl*) histones were obtained from The Histone Source and refolded as described in Luger et al, 1994 (Luger et al. 1997). 147 bp DNA was purified and assembled into tetrasomes using established protocols (Luger et al. 1997).

mNeonGreen was sub-cloned into pET21d-GSP1(1-179, Q71L) from pL0M-S-mNeonGreen-EC18153. pL0M-S-mNeonGreen-EC18153 was a gift from Julian Hibberd (RRID:Addgene 137075). mNeonGreen-GSP1 was expressed in Rosetta(DE3)pLysS cells using 2 L of LB media with ampicillin for selection. The cells were induced with 0.25 mM IPTG for 12 h at 18°C. Protein

was purified as for GSP1. H2A-K119C was labeled with XFD488 and prepared according to the manufacturer's protocol.

Pull-down Binding Assays

Pull-down binding assays were performed by immobilizing purified His_6MBP or His_6MBP-Kap114 on amylose resin (New England BioLab). Resin was stored in Binding Assay (BA) buffer containing 20 mM Tris-HCl pH 7.5, 150 mM NaCl, 10% (v/v) glycerol and 2 mM DTT forming a 50% amylose resin BA slurry. 100 µL of slurry with a total solution volume of 50 µL BA buffer was brought up to a total solution volume of 100 µL with a final concentration of 10 µM His_6MBP or His_6MBP-Kap114, 50 µM *Sc*H2A-H2B, and/or 50 µM RanGTP. RanGTP was added after a 30 min pre-incubation period of the other components and equilibrated for another 30 min at room temperature. Amylose resin was pelleted at 16,000 RCF for 1 min at 4°C using an Eppendorf Centrifuge 5415 R and washed 3 times with 600 µL of BA buffer stored at 4°C with excess solution carefully aspirated. 100 µL of 2x Laemmli sample buffer was added, and BA samples were boiled for 5 min. 10 µL of sample was loaded onto a 12% SDS-PAGE gel. Gels were visualized using Coomassie stain.

Electrophoretic Mobility Shift Assays

For Electromobility Shift Assays (EMSAs) with Imp9, one component was held constant at 10 µM while the other was titrated. For EMSAs with Kap114, one component was held constant at 5 µM, while the other was titrated. Proteins were dialyzed into the same buffer overnight (20 mM HEPES, pH 7.5, 150 mM NaCl, 2 mM MgAcetate, 2 mM Tris(2-carboxyethyl)phosphine hydrochloride (TCEP), 10% (v/v) glycerol). Samples were separated by 5% native PAGE. Gels were run for 100 min at 150 V at 4℃ in 0.5x TBE (40 mM Tris-HCl pH 8.4, 45 mM boric acid, 1 mM Ethylenediaminetetraacetic acid (EDTA)). Gels were stained with Coomassie. Gel shown was one of ≥ 3 repeats.

Analytical Ultracentrifugation

Sedimentation velocity experiments were performed as described in Padavannil et al. Individual proteins were dialyzed into Analytical Ultracentrifugation (AUC) buffer containing 20 mM Tris-HCl pH 7.5, 150 mM NaCl, 2 mM $MgCl_2$ and 2 mM TCEP (Padavannil et al. 2019). 500 µL of AUC sample was equilibrated overnight at 4°C. The AUC sample chamber contained 400 µL of the following: 1) 3 µM Kap114, 2) 10 µM ScH2A-H2B, 3) 10 µM RanGTP, 4) 3 µM Kap114 + 3 µM H2A-H2B, 5) 3 µM Kap114 + 3 µM RanGTP, 6) 3 µM Kap114 + 3 µM H2A-H2B + 10 µM RanGTP.

Sedimentation coefficients were measured by monitoring absorbance at 280 nm in a Beckman-Coulter Optima XL-1 Analytical Ultracentrifuge. The Beckman data time stamps were corrected using REDATE (Zhao et al. 2013). SEDNTERP was used to calculate the buffer density, buffer viscosity, and protein partial-specific volumes (Laue et al. 1992). SEDFIT was used to calculate sedimentation coefficient distributions c(S) where the regularization calculated a confidence level of 0.68 was used, time-independent noise elements were accounted for, and at a resolution of 100 (Schuck 2000). SEDFIT was also used to obtain the sedimentation coefficient by integration of c(S) and the frictional ratios by refining the fit of the model. The data were plotted using GUSSI (Brautigam 2015).

DNA Competition Assays

Imp9, Kap114, Imp9•RanGTP, or Kap114•RanGTP were titrated at various molar equivalents of *Xl*H2A-H2B where H2A-H2B was in a 7:1 complex with 147 bp Widom 601 DNA (10.5 µM H2A-H2B and 1.5 µM DNA). Binary complexes were equimolar Imp9 and RanGTP or Kap114 and RanGTP added together without further purification. Proteins were dialyzed in the same buffer overnight (20 mM HEPES, pH 7.5, 300 mM NaCl, 2 mM MgAcetate, 2 mM TCEP, 10% (v/v) glycerol). Samples were separated by 5% native PAGE. Gels were run for 75 min at 150 V at 4 ℃ in 0.5x TBE. Gels were stained with ethidium bromide and then Coomassie. Gel shown was one of ≥ 3 repeats.

Cryo-EM Specimen Preparation

For Kap114•H2A-H2B and Kap114•RanGTP, individual proteins were buffer exchanged into cryo-EM buffer containing 20 mM Tris-HCl pH 7.5, 300 mM NaCl, 2 mM $MgCl_2$ and 1 mM TCEP and flash frozen at 8 mg/mL. Kap114•H2A-H2B and Kap114•RanGTP were made by mixing 20 µL of Kap114 with 5 µL of *Sc*H2A-H2B or 4.5 µL RanGTP, resulting in a 1 Kap114 to 1.2 H2A-H2B or RanGTP molar ratio at 8 mg/mL. Kap114 complexes were diluted two-fold with cryo-EM buffer plus NP-40 (final concentration of 0.1% (w/v). Samples of Imp9•RanGTP were buffer exchanged into 50 mM Tris-HCl pH 7.5, 150 mM NaCl and 0.1% (w/v) NP-40 at a final protein concentration of 3 mg/ml. 4 µL of Kap114•H2A-H2B/RanGTP or 3.5 µL of Imp9•RanGTP was applied to a 300 mesh copper grid (Quantifoil R1.2/1.3) that was glow-discharged using a PELCO easiGlow glow discharge apparatus for 30 mA/30 s on top of a metal grid holder (Ted Pella). Excess sample was blotted 3 s before plunge-freezing in a ThermoFisher Vitrobot System at 4°C with 95% humidity.

RanGTP•Kap114•H2A-H2B was crosslinked on a Superdex 200 10/300 Increase column equilibrated with cryo-EM buffer. We injected 500 µL of 0.05% (w/v) glutaraldehyde with 3 mL of buffer followed by 500 µL of an equimolar mix of RanGTP, Kap114, and H2A-H2B. We collected 0.5 mL fractions. The ternary complex was concentrated to 8.6 mg/mL and was flash frozen in liquid nitrogen. The complex was diluted two-fold with cryoEM buffer plus Tween-20 (final concentration of 0.00125% (w/v)). The grid was glow-discharged, blotted, and plunge-frozen in a similar manner as the binary complexes.

Cryo-EM Data Collection

Cryo-EM data for Kap114•H2A-H2B and Kap114•RanGTP were collected at the Pacific Northwest Cryo-EM Center on a Titan Krios at 300 kV with a Gatan K3 detector in correlated double sampling super-resolution mode at a magnification of 81,000x corresponding to a pixel size of 0.5295 Å. Each movie was recorded for a total of 58 frames over 3.475 s with an exposure rate of 15 electrons/pixel/s. Datasets were collected using SerialEM (Mastronarde 2005) software with a defocus range of -0.8 and -2.5 µm.

Cryo-EM data collection for Imp9•RanGTP and RanGTP•Kap114•H2A-H2B were collected at the UT Southwestern Cryo-Electron Microscopy Facility on a Titan Krios at 300 kV with a Gatan K3 detector in correlated double sampling super-resolution mode at a magnification of 105,000x corresponding to a pixel size of 0.415 Å. Each movie was recorded for a total of 60 frames over 5.4 s with an exposure rate of 7.8 electrons/pixel/s. The datasets were collected using SerialEM (Mastronarde, 2005) software with a defocus range of -0.9 and -2.4 µm.

Cryo-EM Data Processing

A total of 9,158 movies were collected for Kap114•H2A-H2B and 5,744 movies were collected for Kap114•RanGTP. Both datasets were processed using cryoSPARC (Punjani et al. 2017) where they were first subjected to Patch Motion Correction (Kap114•H2A-H2B unbinned and Kap114•RanGTP binned twice) and Patch CTF Estimation. The Blob Picker was implemented on 50 micrographs to pick all possible particles with little bias and this small set of particles were subjected to 2D Classification to generate 2D templates where a subset of templates was used in Template Picker. 7,006,373 particles were picked in Kap114•H2A-H2B dataset, and 7,640,457 particles were picked in Kap114•RanGTP dataset. 671,257 particles of Kap114•H2A-H2B and 953,500 particles of Kap114•RanGTP were selected after five rounds of 2D Classification. The Kap114•H2A-H2B particles were then sorted into four 3D classes while the Kap114•RanGTP

particles were sorted into six 3D classes using Ab-initio reconstruction followed by Heterogeneous Refinement. The particles from two Kap114•H2A-H2B 3D classes were combined to give 554,529 particles for Non-uniform Refinement which yielded a 3.21 Å resolution map. Three classes of Kap114•RanGTP - Class 1 with 277,305 particles, Class 2 with 258,006 particles and Class 3 with 259,220 particles - were individually subjected to Non-uniform Refinement. We analyzed the local resolution at a 0.5 FSC threshold and determined that Class 1 was the best for model building.

4,767 movies were collected for the RanGTP•Kap114•H2A-H2B complex. This dataset was also processed using cryoSPARC. The movies were subjected to Patch Motion Correction (binned twice) and Patch CTF Estimation. Generation of templates was performed as for the binary complexes and 3,401,608 particles were extracted from the Template Picks. After five rounds of 2D Classification, 604,835 particles were further processed into five Ab-Initio classes and five Heterogeneous Refinement classes. Two of the five classes contained the complex of interest and were subjected to another round of Ab-Initio and Heterogeneous Refinement which generated four new classes. From there, three classes were chosen Non-uniform Refinement: Class 1 with 3.50 Å resolution using 114,232 particles, Class 2 with 3.49 Å resolution using 95,715 particles, and Class 3 with 3.28 Å resolution using 134,915 particles. All maps had local resolution analyzed at a 0.5 FSC threshold, and Class 3 was the best one for model building.

4,920 movies were collected for Imp9•RanGTP and processed using cryoSPARC. A ½ F-crop factor was applied during motion correction followed by patch CTF estimation. A small set of ~20 frames was used to generate the initial template for particle picking. 2,474,170 particles were initially extracted from all the micrographs. The first round of 2D classification produced 904,566 particles that were subjected to another three rounds of 2D classification. 232,798 particles were included for Ab-Initio modeling followed by heterogeneous refinement. Non-uniform refinement was carried out to generate the final 3.7 Å resolution map.

Cryo-EM Model Building, Refinement, and Analysis

The Kap114 proteins in both Kap114•H2A-H2B and Kap114•RanGTP structures were built using coordinates of unliganded Kap114 from the crystal structure PDB 6AHO (Liao et al. 2020). The *Sc*H2A-H2B in Kap114•H2A-H2B was built using *Xl*H2A-H2B coordinates from the Imp9•H2A-H2B crystal structure PDB 6N1Z (Padavannil et al. 2019) and the RanGTP in Kap114•RanGTP built using coordinates of canine Ran in Kap121•RanGTP crystal structure PDB 3W3Z (Kobayashi and Matsuura 2013). The Imp9•RanGTP structure was built using coordinates from PDB 6N1Z

(Padavannil et al. 2019) and PDB 3W3Z (Kobayashi et al. 2013). The RanGTP•Kap114•H2A-H2B complex used Kap114 h1-h15 and RanGTP from Kap114•RanGTP model, and Kap114 h16-h20 and H2A-H2B from Kap114•H2A-H2B. All the models were roughly docked into the map using UCSF Chimera (Pettersen et al. 2004) and then subjected to real-space refinement with global minimization and rigid body restraints on Phenix (Adams et al. 2010). The resulting models were then manually rebuilt and refined using Coot (Emsley and Cowtan 2004), further corrected using ISOLDE (Croll 2018) on UCSF ChimeraX (Goddard et al. 2018), and subjected to another round of refinement in Phenix. Structure interfaces were analyzed using ENDscript 2.0 (Robert and Gouet 2014) with contacts cut-off of 4 Å. These contacts were then manually curated and mapped onto a multiple sequence alignment generated by MAFFT (Katoh and Standley 2013) and visualized by ESPript 3.0 (Robert and Gouet 2014). We used PyMOL version 2.5 for 3D structure analysis (Schrödinger, http://www.pymol.org/pymol).

Hydrogen-Deuterium Exchange Mass Spectrometry

Samples were prepared from 25 µM stocks of Imp9, *Xl*H2A-H2B, RanGTP, Imp9•H2A-H2B (1:1), Imp9•RanGTP (1:0.8), and RanGTP•Imp9•H2A-H2B (0.8:1:1) in 20 mM HEPES pH 7.5, 200 mM NaCl, 2 mM $Mg(CH_3COO)_2•4H_2O$, 2 mM TCEP, 10% (v/v) glycerol, pH 7.5. These stocks were equilibrated at 25°C for 20 min. Control samples were diluted 1:24 with this buffer containing H_2O. For exchange samples, the same buffer containing D_2O was used for 1:24 dilution (pH_{read} = 7.1 at 25°C; final D_2O of 96%). Exchange proceeded at 25°C for 10, 10^2, 10^3, or 10^4 s. Exchange was quenched by mixing samples 1:1 with cooled 0.8% (v/v) formic acid, 2 M urea, pH 1.7 (1:1 mix had a final pH of 2.3 at 0°C) and flash frozen in liquid nitrogen. Samples were prepared in triplicate and stored at −80°C.

Samples were thawed for 50 s immediately prior to injection into a Waters™ HDX manager in line with a SYNAPT G2-Si. In the HDX manager, samples were digested by *Sus scrofa* Pepsin A (Waters™ Enzymate BEH) at 15°C and the peptides trapped on a C4 pre-column (Waters™ Acquity UPLC Protein BEH C4) at 1°C using a flowrate of 100 µl/min for 3 min. The chromatography buffer was 0.1% (v/v) formic acid. Peptides were separated over a C18 column (Waters™ Acquity UPLC BEH) at 1°C and eluted with a linear 3-40% (v/v) acetonitrile gradient using a flowrate of 40 µl/min for 7 min. Samples were injected in a random order.

Mass spectrometry data were acquired using positive ion mode in either HDMS or $HDMS^E$ mode. Peptide identification of water-only control samples was performed using data-independent acquisition in $HDMS^E$ mode. Peptide precursor and fragment data were collected via collision-

induced dissociation at low (6 V) and high (ramping 22-44 V) energy. HDMS mode was used to collect low energy ion data for all deuterated samples. All samples were acquired in resolution mode. Capillary voltage was set to 2.4 kV for the sample sprayer. Desolvation gas was set to 650 L/h at 175°C. The source temperature was set to 80°C. Cone and nebulizer gas was flowed at 90 L/h and 6.5 bar, respectively. The sampling cone and source offset were both set to 30 V. Data were acquired at a scan time of 0.4 s with a range of 100–2000 m/z. Mass correction was done using [Glu1]-fibrinopeptide B as a reference. For ion mobility, the wave velocity was 700 ms^{-1} and the wave height was 40 V.

Raw data of Imp9, H2A-H2B, and RanGTP water-only controls were processed by PLGS (Waters™ Protein Lynx Global Server 3.0.3) using a database containing *S. scrofa* Pepsin A, *Sc*RanGTP**,** *Xl*H2A-H2B, and human Imp9. In PLGS, the minimum fragment ion matches per peptide was 3 and methionine oxidation was allowed. The low and elevated energy thresholds were 250 and 50 counts, respectively, and overall intensity threshold was 750 counts. DynamX 3.0 was used to search the deuterated samples for peptides with 0.3 products per amino acid and 1 consecutive product found in 2 out of 4-5 controls. Data were manually curated. Structural images were made using scripts from DynamX in PyMOL version 2.5 (Schrödinger, http://www.pymol.org/pymol); and heatmaps were made using in-house Python scripts.

To allow access to the HDX data from this study, the HDX data summary table (Figure 4 – Supplement Table 3) and the HDX state data tables (Figure 4 – Supplement Table 4, 5, 6) are included. Theoretical maximum D-uptake used in percent calculations was determined as follows: 0.96×(residues in peptide – 1 for N-terminal residue – the number of prolines not at the N-terminal position). Back exchange was calculated using peptides from the Imp9, H2A-H2B, or RanGTP only sample that had plateaued (<2% difference in D-uptake at 10^3 and 10^4 s) and had a D-uptake >40%. The number reported in Figure 4 - Supplement Table 3 is (100 – the average % D-uptake for these peptides at 10^4 s). The number of peptides used in the calculation was 83, 16, 6, and 9 for Imp9, H2A, H2B, and RanGTP, respectively. The raw mass spectrometry data are available from ProteomeXchange via the PRIDE partner repository with identifier PXD037571 (Perez-Riverol et al. 2016; Deutsch et al. 2020; Perez-Riverol et al. 2022).

Fluorescent Polarization

Fluorescence polarization (FP) assays were performed in a 384-well format as previously described (J. M. Baumhardt et al. 2020; Wing, Fung, and Chook 2022). Kap114, Imp9 and H2A-

H2B were dialyzed overnight into 20 mM HEPES pH 7.5, 150 mM NaCl, 2 mM $MgCl_2$, 2 mM TCEP, 10% (v/v) glycerol. 4 μM Kap114 or 4 μM Imp9 were serially diluted with buffer and mixed with 40 nM mNeonGreen-RanGTP (1:1 volume with final volume of 15 μL). 20 μM Kap114 or 20 μM Imp9 were similarly serially diluted in the presence of 20 μM H2A-H2B and mixed with 40 nM mNeonGreen-RanGTP. Triplicate reactions were analyzed in black-bottom plates (Corning) and data were collected in a CLARIOstar plus plate reader (BMG Labtech) equipped with dichroic filter LP 504. Measurement was performed with top optics with an excitation range of 482-16 nm and emission range of 530-40 nm, 50 flashes per well at focal height of 5.1 mm with a 0.1 s settling time. Gain was adjusted using an empty well with target mP of 200 and kept constant for the rest of the measurements. Data were analyzed in PALMIST (Scheuermann et al. 2016) and fitted with a 1:1 binding model, using error surface projection method to calculate the 95% confidence intervals of the fitted data. Fitted data were exported and plotted in GUSSI (Brautigam 2015).

Nucleosome Assembly Assays

Tetrasomes containing *Xl*$(H3\text{-}H4)_2$ and 147 bp Widom 601 DNA were reconstituted as described in Dyer et al (Dyer et al. 2003). To monitor nucleosome assembly, tetrasomes were held constant at 1.25 μM and H2A-H2B or pre-formed complexes of Imp9•H2A-H2B (1:1), RanGTP•Imp9•H2A-H2B (1:1:1), Kap114•H2A-H2B (1:1), or RanGTP•Kap114•H2A-H2B (1:1:1) were titrated at 2 and 3 molar equivalents. Proteins were dialyzed into the same buffer overnight (20 mM HEPES, pH 7.5, 150 mM NaCl, 2 mM MgAcetate, 2 mM TCEP, 10% (v/v) glycerol). Samples were separated by 5% native PAGE. Gels were run for 75 min at 150 V at 4℃ in 0.5x TBE. Gels were stained with ethidium bromide and then Coomassie. Gel shown was one of ≥ 3 repeats.

Acknowledgments

We thank Abhilash Padavannil for the important biochemical studies that led to this work, and Divyasri Damacharla for initial HDX protocols. A portion of this research was supported by NIH grant U24GM129547 and performed at the PNCC at OHSU and accessed through EMSL (grid.436923.9), a DOE Office of Science User Facility sponsored by the Office of Biological and Environmental Research. We thank the Structural Biology Laboratory and the Cryo-EM Facility at UTSW, which are partially supported by grant RP170644 from the Cancer Prevention & Research Institute of Texas (CPRIT), for cryo-EM studies for their assistance with cryo-EM data collection. We thank Chad Brautigam and the Macromolecular Biophysics Resource at UTSW for training and use of their Analytical Ultracentrifuge. We also thank the Erzberger lab for the use of their equipment for fluorescence polarization experiments. We acknowledge The Histone Source at

Colorado State University for generating the *Xl* and *Sc* histone H2A and H2B proteins used in this study. This work was funded by NIGMS of NIH under Awards R35GM141461 (Y.M.C.), R01GM069909 (Y.M.C.), R35GM133751 (S.D.), the Welch Foundation Grants I-1532 (Y.M.C.), AT-2059-20210327 (S.D.), NSF MRI 2018188 (S.D.), support from the Alfred and Mabel Gilman Chair in Molecular Pharmacology, Eugene McDermott Scholar in Biomedical Research (Y.M.C.), Mary Kay International Postdoctoral Fellowship (N.E.B.) and the Gilman Special Opportunities Award (H.Y.J.F.).

Competing Interest

No competing interests declared.

References

Adams, Paul D., Pavel v. Afonine, Gábor Bunkóczi, Vincent B. Chen, Ian W. Davis, Nathaniel Echols, Jeffrey J. Headd, et al. 2010. "PHENIX: A Comprehensive Python-Based System for Macromolecular Structure Solution." *Acta Crystallographica. Section D, Biological Crystallography* 66 (Pt 2): 213–21. https://doi.org/10.1107/S0907444909052925.

Aguilar-Gurrieri, Carmen, Amédé Larabi, Vinesh Vinayachandran, Nisha A Patel, Kuangyu Yen, Rohit Reja, Ima-O Ebong, et al. 2016. "Structural Evidence for Nap1-dependent H2A–H2B Deposition and Nucleosome Assembly." *The EMBO Journal* 35 (13). https://doi.org/10.15252/embj.201694105.

Avvakumov, Nikita, Amine Nourani, and Jacques Côté. 2011. "Histone Chaperones: Modulators of Chromatin Marks." *Molecular Cell* 41 (5): 502–14. https://doi.org/10.1016/J.MOLCEL.2011.02.013.

Baumhardt, Jordan, and Yuh Min Chook. 2018. "Structures of Importins and Exportins," 113–49. https://doi.org/10.1007/978-3-319-77309-4_6.

Baumhardt, Jordan M., Janek S. Walker, Yoonji Lee, Binita Shakya, Chad A. Brautigam, Rosa Lapalombella, Nick Grishin, and Yuh Min Chook. 2020. "Recognition of Nuclear Export Signals by CRM1 Carrying the Oncogenic E571K Mutation." *Molecular Biology of the Cell* 31 (17): 1879–91. https://doi.org/10.1091/MBC.E20-04-0233.

Bednenko, Janna, Gino Cingolani, and Larry Gerace. 2003. "Nucleocytoplasmic Transport: Navigating the Channel." *Traffic (Copenhagen, Denmark)* 4 (3): 127–35. https://doi.org/10.1034/J.1600-0854.2003.00109.X.

Bernardes, Natália Elisa, Ho Yee Joyce Fung, Yang Li, Zhe Chen, and Yuh Min Chook. 2022. "Structure of IMPORTIN-4 Bound to the H3-H4-ASF1 Histone-Histone Chaperone Complex." *Proceedings of the National Academy of Sciences of the United States of America* 119 (38): e2207177119. https://doi.org/10.1073/PNAS.2207177119/SUPPL_FILE/PNAS.2207177119.SAPP.PDF.

Brautigam, Chad A. 2015. "Calculations and Publication-Quality Illustrations for Analytical Ultracentrifugation Data." *Methods in Enzymology* 562: 109–33. https://doi.org/10.1016/BS.MIE.2015.05.001.

Chen, Xu, Sheena D'Arcy, Catherine A. Radebaugh, Daniel D. Krzizike, Holli A. Giebler, Liangquan Huang, Jennifer K. Nyborg, Karolin Luger, and Laurie A. Stargell. 2016. " Histone Chaperone Nap1 Is a Major Regulator of Histone H2A-H2B Dynamics at the Inducible GAL Locus ." *Molecular and Cellular Biology* 36 (8): 1287–96. https://doi.org/10.1128/MCB.00835-15/SUPPL_FILE/ZMB999101198SO1.PDF.

Chook, Yuh Min, and Günter Blobel. 1999. "Structure of the Nuclear Transport Complex Karyopherin-Beta2-Ran x GppNHp." *Nature* 399 (6733): 230–37. https://doi.org/10.1038/20375.

Cook, Atlanta, Fulvia Bono, Martin Jinek, and Elena Conti. 2007. "Structural Biology of Nucleocytoplasmic Transport." *Annual Review of Biochemistry* 76: 647–71. https://doi.org/10.1146/ANNUREV.BIOCHEM.76.052705.161529.

Corbeski, Ivan, Xiaohu Guo, Bruna v. Eckhardt, Domenico Fasci, Wouter Wiegant, Melissa A. Graewert, Kees Vreeken, et al. 2022. "Chaperoning of the Histone Octamer by the Acidic Domain of DNA Repair Factor APLF." *Science Advances* 8 (30): 517. https://doi.org/10.1126/SCIADV.ABO0517/SUPPL_FILE/SCIADV.ABO0517_SM.PDF.

Croll, Tristan Ian. 2018. "ISOLDE: A Physically Realistic Environment for Model Building into Low-Resolution Electron-Density Maps." *Acta Crystallographica Section D: Structural Biology* 74 (6): 519–30. https://doi.org/10.1107/S2059798318002425/IC5101SUP2.MP4.

Dabin, Juliette, and Sophie E. Polo. 2017. "Choreography of Parental Histones in Damaged Chromatin." *Https://Doi.Org/10.1080/19491034.2017.1292192* 8 (3): 255–60. https://doi.org/10.1080/19491034.2017.1292192.

D'Arcy, Sheena, Kyle W. Martin, Tanya Panchenko, Xu Chen, Serge Bergeron, Laurie A. Stargell, Ben E. Black, and Karolin Luger. 2013. "Chaperone Nap1 Shields Histone Surfaces Used in a Nucleosome and Can Put H2A-H2B in an Unconventional Tetrameric Form." *Molecular Cell* 51 (5): 662–77. https://doi.org/10.1016/J.MOLCEL.2013.07.015.

Deutsch, Eric W., Nuno Bandeira, Vagisha Sharma, Yasset Perez-Riverol, Jeremy J. Carver, Deepti J. Kundu, David García-Seisdedos, et al. 2020. "The ProteomeXchange Consortium in 2020: Enabling 'big Data' Approaches in Proteomics." *Nucleic Acids Research* 48 (D1): D1145–52. https://doi.org/10.1093/NAR/GKZ984.

Dyer, Pamela N., Raji S. Edayathumangalam, Cindy L. White, Yunhe Bao, Srinivas Chakravarthy, Uma M. Muthurajan, and Karolin Luger. 2003. "Reconstitution of Nucleosome Core Particles from Recombinant Histones and DNA." *Methods in Enzymology* 375: 23–44. https://doi.org/10.1016/S0076-6879(03)75002-2.

Elsässer, Simon J., and Sheena D'Arcy. 2012. "Towards a Mechanism for Histone Chaperones." *Biochimica et Biophysica Acta (BBA) - Gene Regulatory Mechanisms* 1819 (3–4): 211–21. https://doi.org/10.1016/J.BBAGRM.2011.07.007.

Emsley, Paul, and Kevin Cowtan. 2004. "Coot: Model-Building Tools for Molecular Graphics." *Acta Crystallographica. Section D, Biological Crystallography* 60 (Pt 12 Pt 1): 2126–32. https://doi.org/10.1107/S0907444904019158.

Fried, H., and U. Kutay. 2003. "Nucleocytoplasmic Transport: Taking an Inventory." *Cellular and Molecular Life Sciences : CMLS* 60 (8): 1659–88. https://doi.org/10.1007/S00018-003-3070-3.

Goddard, Thomas D., Conrad C. Huang, Elaine C. Meng, Eric F. Pettersen, Gregory S. Couch, John H. Morris, and Thomas E. Ferrin. 2018. "UCSF ChimeraX: Meeting Modern Challenges in Visualization and Analysis." *Protein Science* 27 (1): 14–25. https://doi.org/10.1002/PRO.3235.

Görlich, D., and U. Kutay. 1999. "Transport between the Cell Nucleus and the Cytoplasm." *Annual Review of Cell and Developmental Biology* 15: 607–60. https://doi.org/10.1146/ANNUREV.CELLBIO.15.1.607.

Görlich, Dirk, Nelly Panté, Ulrike Kutay, Ueli Aebi, and F. Ralf Bischoff. 1996. "Identification of Different Roles for RanGDP and RanGTP in Nuclear Protein Import." *The EMBO Journal* 15 (20): 5584–94. https://doi.org/10.1002/j.1460-2075.1996.tb00943.x.

Grünwald, Marlene, and Fulvia Bono. 2011. "Structure of Importin13–Ubc9 Complex: Nuclear Import and Release of a Key Regulator of Sumoylation." *The EMBO Journal* 30 (2): 427–38. https://doi.org/10.1038/EMBOJ.2010.320.

Gunjan, Akash, Johanna Paik, and Alain Verreault. 2006. "The Emergence of Regulated Histone Proteolysis." *Current Opinion in Genetics & Development* 16 (2): 112–18. https://doi.org/10.1016/J.GDE.2006.02.010.

Hahn, Silvia, and Gabriel Schlenstedt. 2011. "Importin β-Type Nuclear Transport Receptors Have Distinct Binding Affinities for Ran-GTP." *Biochemical and Biophysical Research Communications* 406 (3): 383–88. https://doi.org/10.1016/j.bbrc.2011.02.051.

Hammond, Colin M., Caroline B. Strømme, Hongda Huang, Dinshaw J. Patel, and Anja Groth. 2017. "Histone Chaperone Networks Shaping Chromatin Function." *Nature Reviews Molecular Cell Biology 2017 18:3* 18 (3): 141–58. https://doi.org/10.1038/nrm.2016.159.

Havugimana, Pierre C., G. Traver Hart, Tamás Nepusz, Haixuan Yang, Andrei L. Turinsky, Zhihua Li, Peggy I. Wang, et al. 2012. "A Census of Human Soluble Protein Complexes." *Cell* 150 (5): 1068–81. https://doi.org/10.1016/J.CELL.2012.08.011.

Huang, Yan, Yaxin Dai, and Zheng Zhou. 2020. "Mechanistic and Structural Insights into Histone H2A-H2B Chaperone in Chromatin Regulation." *The Biochemical Journal* 477 (17): 3367–86. https://doi.org/10.1042/BCJ20190852.

Jäkel, Stefan, José-Manuel Mingot, Petra Schwarzmaier, Enno Hartmann, and Dirk Görlich. 2002. "Importins Fulfil a Dual Function as Nuclear Import Receptors and Cytoplasmic Chaperones for Exposed Basic Domains." *The EMBO Journal* 21 (3): 377–86. https://doi.org/10.1093/EMBOJ/21.3.377.

Jiang, Kai, Lenka Rezabkova, Shasha Hua, Qingyang Liu, Guido Capitani, A. F.Maarten Altelaar, Albert J.R. Heck, Richard A. Kammerer, Michel O. Steinmetz, and Anna Akhmanova. 2017. "Microtubule Minus-End Regulation at Spindle Poles by an ASPM-Katanin Complex." *Nature Cell Biology* 19 (5): 480–92. https://doi.org/10.1038/NCB3511.

Kalashnikova, Anna A., Mary E. Porter-Goff, Uma M. Muthurajan, Karolin Luger, and Jeffrey C. Hansen. 2013. "The Role of the Nucleosome Acidic Patch in Modulating Higher Order Chromatin Structure." *Journal of The Royal Society Interface* 10 (82). https://doi.org/10.1098/RSIF.2012.1022.

Katoh, Kazutaka, and Daron M. Standley. 2013. "MAFFT Multiple Sequence Alignment Software Version 7: Improvements in Performance and Usability." *Molecular Biology and Evolution* 30 (4): 772–80. https://doi.org/10.1093/MOLBEV/MST010.

Keck, Kristin M., and Lucy F. Pemberton. 2012. "Histone Chaperones Link Histone Nuclear Import and Chromatin Assembly." *Biochimica et Biophysica Acta - Gene Regulatory Mechanisms* 1819 (3–4): 277–89. https://doi.org/10.1016/j.bbagrm.2011.09.007.

Kimura, Makoto, Yuriko Morinaka, Kenichiro Imai, Shingo Kose, Paul Horton, and Naoko Imamoto. 2017. "Extensive Cargo Identification Reveals Distinct Biological Roles of the 12 Importin Pathways." *ELife* 6 (January). https://doi.org/10.7554/ELIFE.21184.

Kobayashi, Junya, and Yoshiyuki Matsuura. 2013. "Structural Basis for Cell-Cycle-Dependent Nuclear Import Mediated by the Karyopherin Kap121p." *Journal of Molecular Biology* 425 (11): 1852–68. https://doi.org/10.1016/J.JMB.2013.02.035.

Kochert, Brent A., Roxana E. Iacob, Thomas E. Wales, Alexandros Makriyannis, and John R. Engen. 2018. "Hydrogen-Deuterium Exchange Mass Spectrometry to Study Protein Complexes." *Methods in Molecular Biology (Clifton, N.J.)* 1764: 153–71. https://doi.org/10.1007/978-1-4939-7759-8_10.

Laue, Thomas M, Bhairavi D Shah, Theresa M Ridgeway, and Sandra L Pelletier. 1992. *Analytical Ultracentrifugation in Biochemistry and Polymer Science*. *Analytical Ultracentrifugation in Biochemistry and Polymer Science*. Cambridge [England] : Royal Society of Chemistry,.

Lee, Soo Jae, Yoshiyuki Matsuura, Sai Man Liu, and Murray Stewart. 2005. "Structural Basis for Nuclear Import Complex Dissociation by RanGTP." *Nature 2005 435:7042* 435 (7042): 693–96. https://doi.org/10.1038/nature03578.

Liao, Chung-Chi, Sahana Shankar, Wen-Chieh Pi, Chih-Chia Chang, Golam Rizvee Ahmed, Wei-Yi Chen, and Kuo-Chiang Hsia. 2020. "Karyopherin Kap114p-mediated Trans-repression Controls Ribosomal Gene Expression under Saline Stress." *EMBO Reports* 21 (7). https://doi.org/10.15252/EMBR.201948324.

Liu, Yang, Keda Zhou, Naifu Zhang, Hui Wei, Yong Zi Tan, Zhening Zhang, Bridget Carragher, Clinton S. Potter, Sheena D'Arcy, and Karolin Luger. 2020. "FACT Caught in the Act of Manipulating the Nucleosome." *Nature*. https://doi.org/10.1038/s41586-019-1820-0.

Luger, Karolin, Armin W. Mäder, Robin K. Richmond, David F. Sargent, and Timothy J. Richmond. 1997. "Crystal Structure of the Nucleosome Core Particle at 2.8 Å Resolution." *Nature*. https://doi.org/10.1038/38444.

Maertens, Goedele N., Nicola J. Cook, Weifeng Wang, Stephen Hare, Saumya Shree Gupta, Ilker Öztop, Kyeong Eun Lee, et al. 2014. "Structural Basis for Nuclear Import of Splicing Factors by Human Transportin 3." *Proceedings of the National Academy of Sciences of the United States of America* 111 (7): 2728–33. https://doi.org/10.1073/PNAS.1320755111/SUPPL_FILE/SM01.MOV.

Makde, Ravindra D., Joseph R. England, Hemant P. Yennawar, and Song Tan. 2010. "Structure of RCC1 Chromatin Factor Bound to the Nucleosome Core Particle." *Nature* 467 (7315): 562–66. https://doi.org/10.1038/NATURE09321.

Mastronarde, David N. 2005. "Automated Electron Microscope Tomography Using Robust Prediction of Specimen Movements." *Journal of Structural Biology* 152 (1): 36–51. https://doi.org/10.1016/J.JSB.2005.07.007.

Mosammaparast, Nima, Courtney S. Ewart, and Lucy F. Pemberton. 2002. "A Role for Nucleosome Assembly Protein 1 in the Nuclear Transport of Histones H2A and H2B." *The EMBO Journal* 21 (23): 6527. https://doi.org/10.1093/EMBOJ/CDF647.

Mosammaparast, Nima, Kelley R. Jackson, Yurong Guo, Cynthia J. Brame, Jeffrey Shabanowitz, Donald F. Hunt, and Lucy F. Pemberton. 2001. "Nuclear Import of Histone H2A and H2B Is Mediated by a Network of Karyopherins." *Journal of Cell Biology* 153 (2): 251–62. https://doi.org/10.1083/jcb.153.2.251.

Mosammaparast, Nima, Brian C. del Rosario, and Lucy F. Pemberton. 2005. "Modulation of Histone Deposition by the Karyopherin Kap114." *Molecular and Cellular Biology* 25 (5): 1764–78. https://doi.org/10.1128/MCB.25.5.1764-1778.2005/ASSET/D6E7358D-5FB0-42D4-BFD3-5C68969511AE/ASSETS/GRAPHIC/ZMB0050548100011.JPEG.

Mühlhäusser, Petra, Eva Christina Müller, Albrecht Otto, and Ulrike Kutay. 2001. "Multiple Pathways Contribute to Nuclear Import of Core Histones." *EMBO Reports* 2 (8): 690. https://doi.org/10.1093/EMBO-REPORTS/KVE168.

Nemergut, M. E., C. A. Mizzen, T. Stukenberg, C. D. Allis, and I. G. Macara. 2001. "Chromatin Docking and Exchange Activity Enhancement of RCC1 by Histones H2A and H2B." *Science* 292 (5521): 1540–43. https://doi.org/10.1126/SCIENCE.292.5521.1540/ASSET/7F39CC6E-5324-4984-BBB5-261DA5EF6948/ASSETS/GRAPHIC/SE2019453003.JPEG.

Obri, Arnaud, Khalid Ouararhni, Christophe Papin, Marie Laure Diebold, Kiran Padmanabhan, Martin Marek, Isabelle Stoll, et al. 2014. "ANP32E Is a Histone Chaperone That Removes H2A.Z from Chromatin." *Nature 2014 505:7485* 505 (7485): 648–53. https://doi.org/10.1038/nature12922.

Padavannil, Abhilash, Prithwijit Sarkar, Seung Joong Kim, Tolga Cagatay, Jenny Jiou, Chad A. Brautigam, Diana R. Tomchick, Andrej Sali, Sheena D'Arcy, and Yuh Min Chook. 2019. "Importin-9 Wraps around the H2A-H2B Core to Act as Nuclear Importer and Histone Chaperone." *ELife* 8 (March). https://doi.org/10.7554/ELIFE.43630.

Pardal, Alonso J., Filipe Fernandes-Duarte, and Andrew J. Bowman. 2019. "The Histone Chaperoning Pathway: From Ribosome to Nucleosome." *Essays in Biochemistry* 63 (1): 29–43. https://doi.org/10.1042/EBC20180055.

Perez-Riverol, Yasset, Jingwen Bai, Chakradhar Bandla, David García-Seisdedos, Suresh Hewapathirana, Selvakumar Kamatchinathan, Deepti J. Kundu, et al. 2022. "The PRIDE Database Resources in 2022: A Hub for Mass Spectrometry-Based Proteomics Evidences." *Nucleic Acids Research* 50 (D1): D543. https://doi.org/10.1093/NAR/GKAB1038.

Perez-Riverol, Yasset, Qing-Wei Xu, Rui Wang, Julian Uszkoreit, Johannes Griss, Aniel Sanchez, Florian Reisinger, et al. 2016. "PRIDE Inspector Toolsuite: Moving Toward a Universal Visualization Tool for Proteomics Data Standard Formats and Quality Assessment of ProteomeXchange Datasets." https://doi.org/10.1074/mcp.O115.050229.

Pettersen, Eric F., Thomas D. Goddard, Conrad C. Huang, Gregory S. Couch, Daniel M. Greenblatt, Elaine C. Meng, and Thomas E. Ferrin. 2004. "UCSF Chimera—A Visualization System for Exploratory Research and Analysis." *Journal of Computational Chemistry* 25 (13): 1605–12. https://doi.org/10.1002/JCC.20084.

Punjani, Ali, John L. Rubinstein, David J. Fleet, and Marcus A. Brubaker. 2017. "CryoSPARC: Algorithms for Rapid Unsupervised Cryo-EM Structure Determination." *Nature Methods 2017 14:3* 14 (3): 290–96. https://doi.org/10.1038/nmeth.4169.

Robert, Xavier, and Patrice Gouet. 2014. "Deciphering Key Features in Protein Structures with the New ENDscript Server." *Nucleic Acids Research* 42 (Web Server issue). https://doi.org/10.1093/NAR/GKU316.

Rothenbusch, Ute, Marc Sawatzki, Yiming Chang, Stefanie Caesar, and Gabriel Schlenstedt. 2012. "Sumoylation Regulates Kap114-Mediated Nuclear Transport." *The EMBO Journal* 31 (11): 2461–72. https://doi.org/10.1038/EMBOJ.2012.102.

Scheuermann, Thomas H., Shae B. Padrick, Kevin H. Gardner, and Chad A. Brautigam. 2016. "On the Acquisition and Analysis of Microscale Thermophoresis Data." *Analytical Biochemistry* 496 (March): 79–93. https://doi.org/10.1016/J.AB.2015.12.013.

Schuck, Peter. 2000. "Size-Distribution Analysis of Macromolecules by Sedimentation Velocity Ultracentrifugation and Lamm Equation Modeling." *Biophysical Journal* 78 (3): 1606–19. https://doi.org/10.1016/S0006-3495(00)76713-0.

Soniat, Michael, and Yuh Min Chook. 2015. "Nuclear Localization Signals for Four Distinct Karyopherin-β Nuclear Import Systems." *The Biochemical Journal* 468 (3): 353–62. https://doi.org/10.1042/BJ20150368.

Straube, Korinna, Jeffrey S. Blackwell, and Lucy F. Pemberton. 2010. "Nap1 and Chz1 Have Separate Htz1 Nuclear Import and Assembly Functions." *Traffic* 11 (2): 185–97. https://doi.org/10.1111/J.1600-0854.2009.001010.X.

Thiriet, C., and J. J. Hayes. 2001. “A Novel Labeling Technique Reveals a Function for Histone H2A/H2B Dimer Tail Domains in Chromatin Assembly in Vivo.” *Genes & Development* 15 (16): 2048–53. https://doi.org/10.1101/GAD.910201.

Tsirkone, Vicky G., Katrien G. Beutels, Jonas Demeulemeester, Zeger Debyser, Frauke Christ, and Sergei v. Strelkov. 2014. “Structure of Transportin SR2, a Karyopherin Involved in Human Disease, in Complex with Ran.” *Acta Crystallographica. Section F, Structural Biology Communications* 70 (Pt 6): 723–29. https://doi.org/10.1107/S2053230X14009492.

Vetter, Ingrid R., Andreas Arndt, Ulrike Kutay, Dirk Görlich, and Alfred Wittinghofer. 1999. “Structural View of the Ran-Importin Beta Interaction at 2.3 A Resolution.” *Cell* 97 (5): 635–46. https://doi.org/10.1016/S0092-8674(00)80774-6.

Weis, Karsten. 2002. “Nucleocytoplasmic Transport: Cargo Trafficking across the Border.” *Current Opinion in Cell Biology* 14 (3): 328–35. https://doi.org/10.1016/S0955-0674(02)00337-X.

Weis, Karsten. 2003. “Regulating Access to the Genome: Nucleocytoplasmic Transport throughout the Cell Cycle.” *Cell* 112 (4): 441–51. https://doi.org/10.1016/S0092-8674(03)00082-5.

Wente, Susan R., and Michael P. Rout. 2010. “The Nuclear Pore Complex and Nuclear Transport.” *Cold Spring Harbor Perspectives in Biology* 2 (10). https://doi.org/10.1101/CSHPERSPECT.A000562.

Wing, Casey E., Ho Yee Joyce Fung, and Yuh Min Chook. 2022. “Karyopherin-Mediated Nucleocytoplasmic Transport.” *Nature Reviews Molecular Cell Biology* 23 (5): 307–28. https://doi.org/10.1038/s41580-021-00446-7.

Woodley, Keith T, and Mark O Collins. 2019. “S-Acylated Golga7b Stabilises DHHC5 at the Plasma Membrane to Regulate Cell Adhesion.” *EMBO Reports* 20 (10). https://doi.org/10.15252/EMBR.201847472.

Zhao, Huaying, Rodolfo Ghirlando, Grzegorz Piszczek, Ute Curth, Chad A. Brautigam, and Peter Schuck. 2013. “Recorded Scan Times Can Limit the Accuracy of Sedimentation Coefficients in Analytical Ultracentrifugation.” *Analytical Biochemistry* 437 (1): 104–8. https://doi.org/10.1016/J.AB.2013.02.011.

Supplement for: Mechanism of RanGTP priming the release of H2A-H2B from Kap114 and Importin-9

Jenny Jiou[#1], Joy M. Shaffer[#2], Natalia E. Bernades[1], Kiran Tripathi[2], Ho Yee J. Fung[1], Oladimeji S. Olaluwoye[2], Juliana Kikumoto Dias[2], Yuh Min Chook*[1], and Sheena D'Arcy*[2]

[1] Department of Pharmacology, University of Texas Southwestern Medical Center, Dallas, United States, 75390

[2] Department of Chemistry and Biochemistry, University of Texas at Dallas, Richardson, United States, 75080

[#] Co-first author

* Corresponding authors

For correspondence:

Sheena.DArcy@utdallas.edu

YuhMin.Chook@utsouthwestern.edu

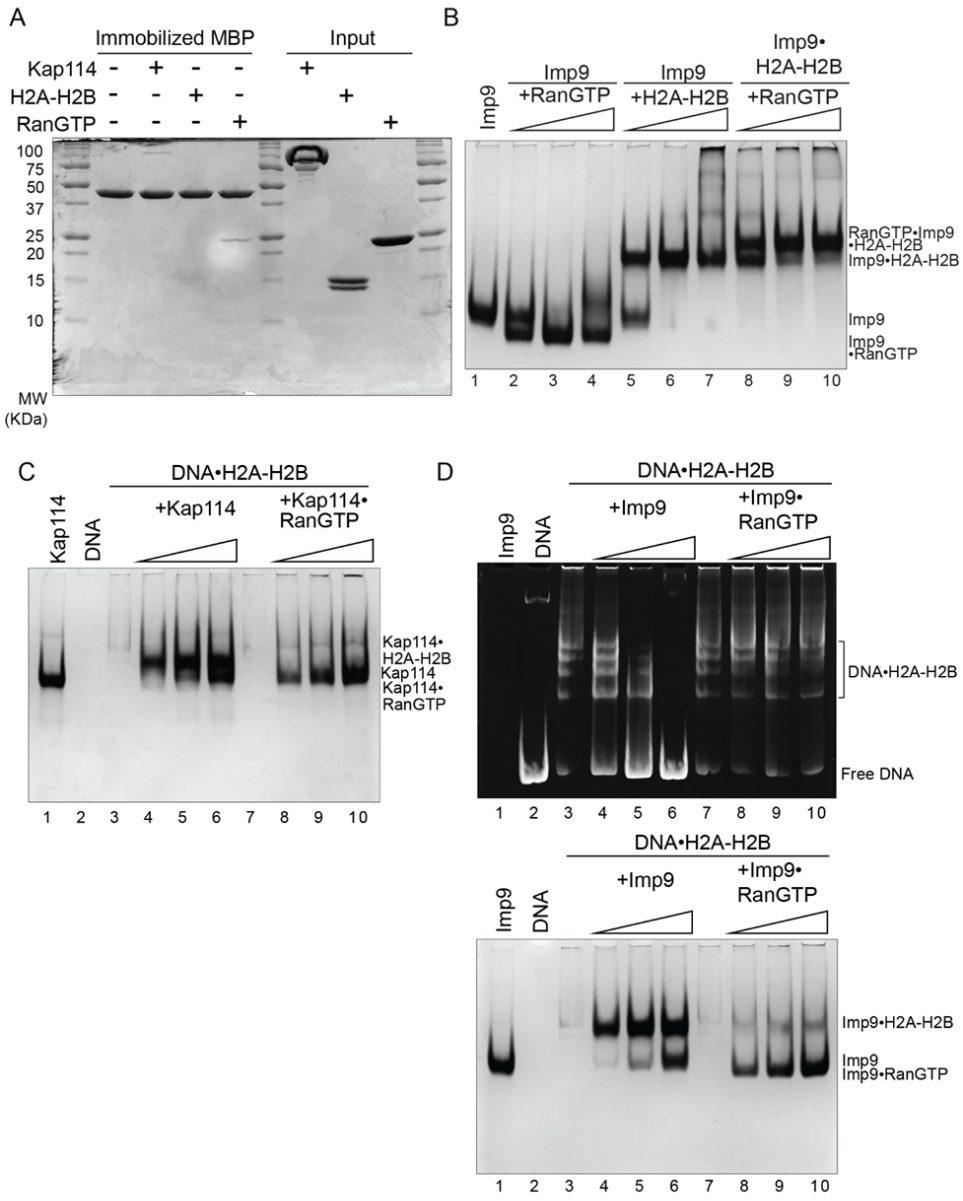

Figure 1 - Supplement 1: (**A**) Pull-down binding assays of immobilized MBP on amylose beads with untagged Kap114, H2A-H2B, and RanGTP added. After extensive washing, bound and input proteins were visualized by Coomassie-stained SDS-PAGE. (**B**) Constant Imp9 (lanes 2-7) was titrated with 0.5, 1, or 1.5 molar ratio of RanGTP (lanes 2-4) or H2A-H2B (lane 5-7). Constant Imp9•H2A-H2B was titrated with 0.5, 1, or 1.5 molar ratio of RanGTP (lanes 8-10). Protein was visualized by Coomassie-stained native PAGE. (**C**) DNA competition assay with Kap114 (lanes 4-6) titrated at 0.5, 1, or 1.5 molar equivalents of H2A-H2B (in a DNA•H2A-H2B 1:7 complex), while Kap114•RanGTP (1:1, lanes 8-10) is titrated at 0.25, 0.5, or 1.0 molar equivalents of H2A-H2B (in a DNA•H2A-H2B 1:7 complex. Native PAGE was visualized with Coomassie staining. Ethidium bromide is shown in ***Figure 1D***. (**D**) DNA competition assay with Imp9 (lanes 4-6) titrated at 0.5, 1, or 1.5 molar equivalents of H2A-H2B (in a DNA•H2A-H2B 1:7 complex), while Imp9•RanGTP (1:1, lanes 8-10) is titrated at 0.25, 0.5, or 1.0 molar equivalents of H2A-H2B (in a DNA•H2A-H2B 1:7 complex. Native PAGE was visualized with ethidium bromide (top) and Coomassie staining (bottom). Source data for A-D is in ***Figure 1 - Supplement 1 - Source Data 1-4*** respectively.

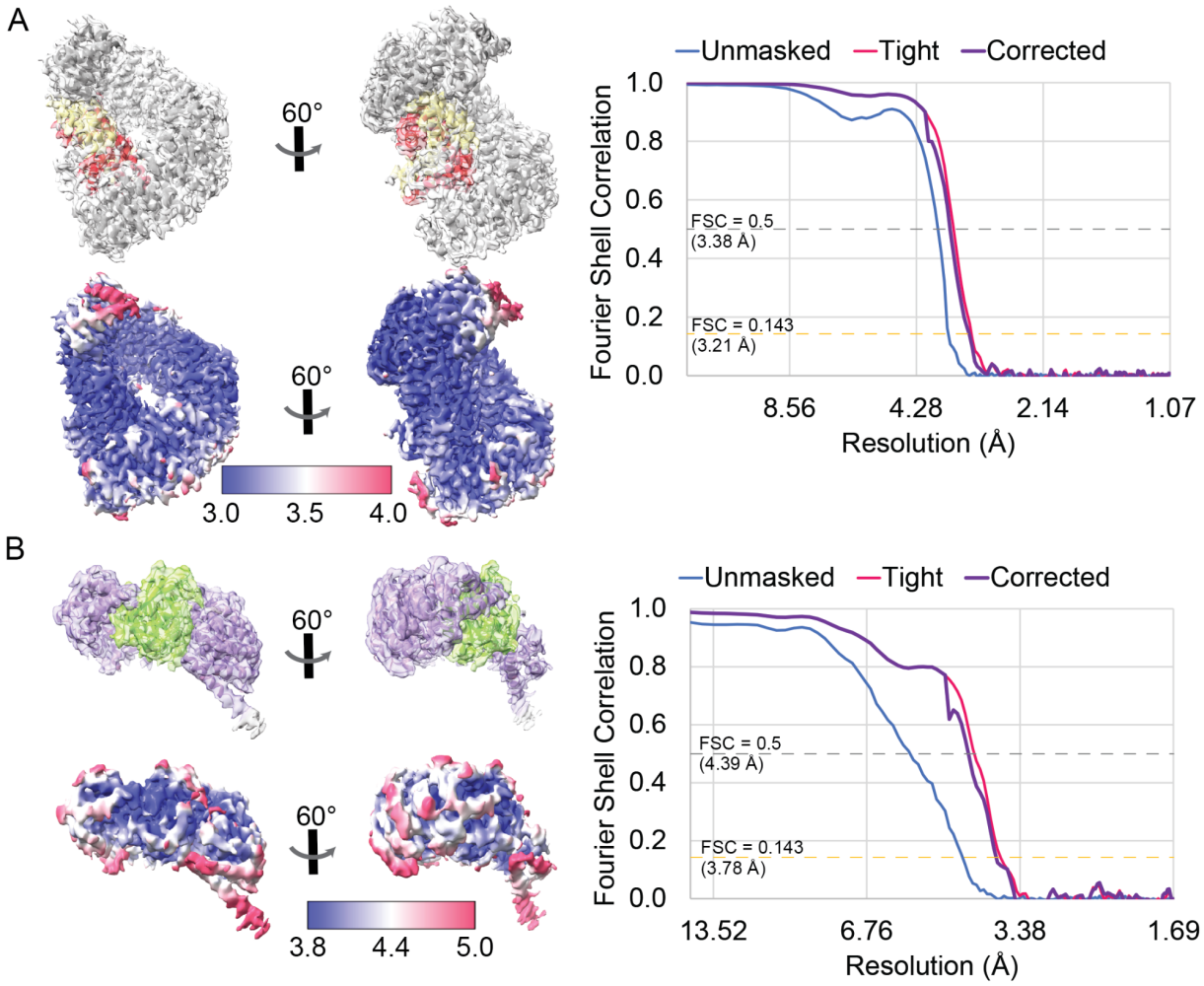

Figure 2 - Supplement 1: (**A**) The Kap114•H2A-H2B model, colored gray•yellow-red, is docked into its map with the local resolution displayed below (Left). The local resolution was colored to show according to the scale displayed. The FSC curves were plotted with Unmasked in blue, Tight in pink, and Corrected in purple (Right). The gold dashed line marks the FSC = 0.143, and the gray dashed line represents FSC = 0.5. (**B**) Imp9•RanGTP model, colored purple•green, is docked into its map - shown with its corresponding local resolution and its FSC curve.

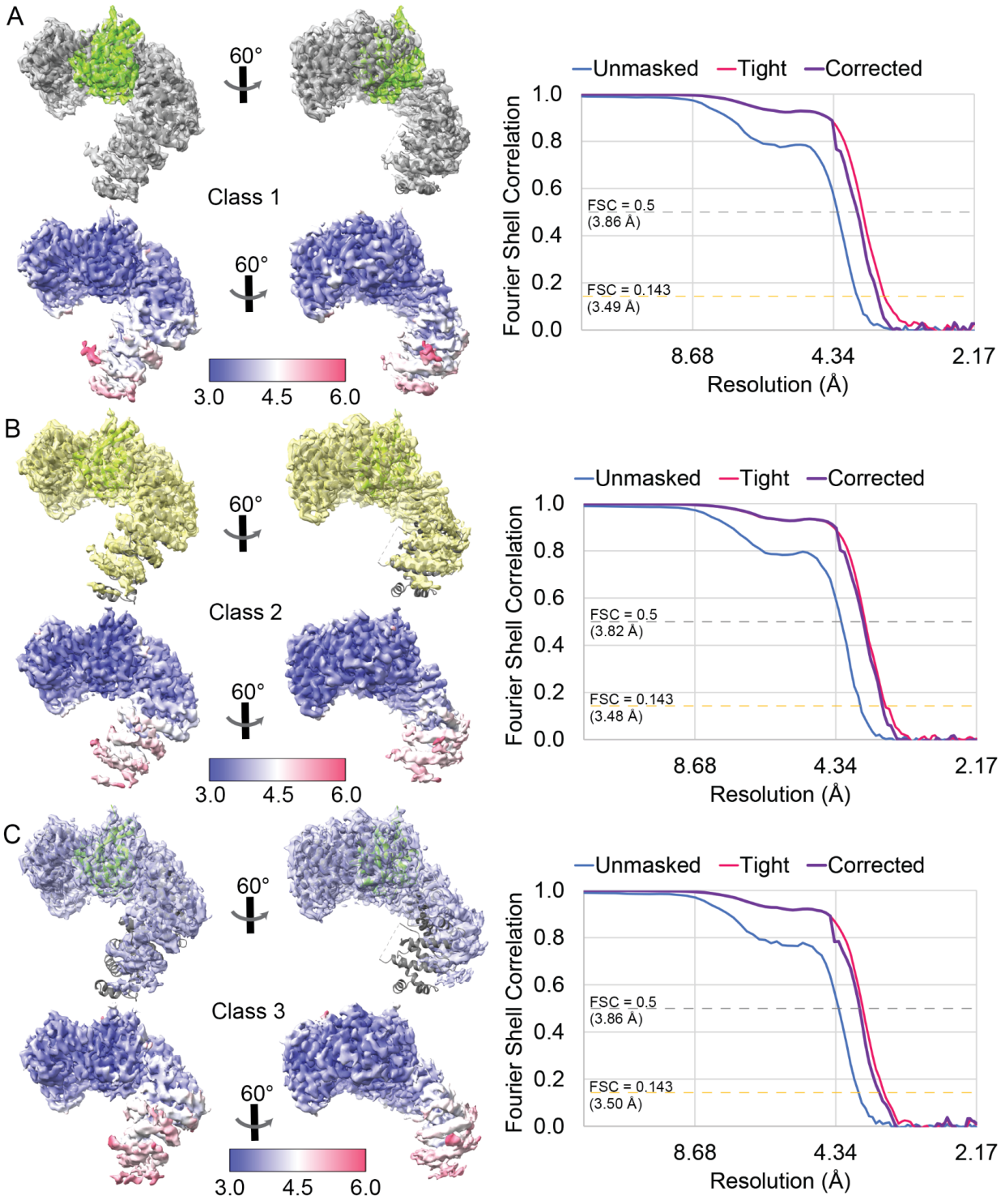

Figure 2 - Supplement 2: (**A**) The Kap114•RanGTP model of Class 1, colored gray•green, is docked into the Class 1 map with the local resolution displayed below (Left). The local resolution was colored according to the scale displayed. The FSC curves were plotted with Unmasked in blue, Tight in pink, and Corrected in purple (Right). The gold dashed line marks the FSC = 0.143, and the gray dashed line represents FSC = 0.5. The same Class 1 model is docked into (**B**) a yellow Class 2 map and (**C**) a light blue Class 3 map - shown with the corresponding local resolution and FSC curve.

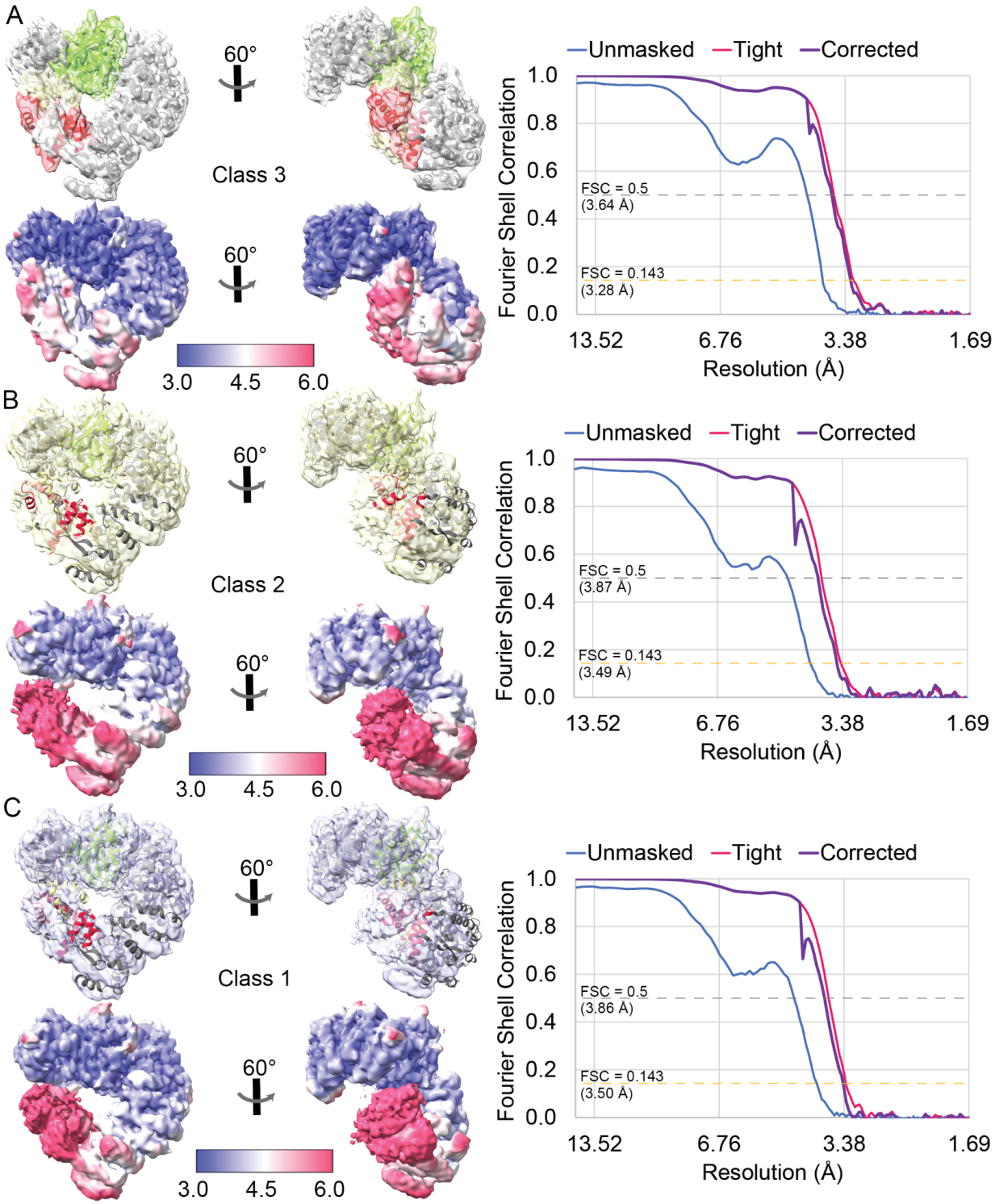

Figure 2 - Supplement 3: (**A**) The RanGTP•Kap114•H2A-H2B model of Class 3, colored green•gray•yellow-red, is docked into the Class 3 map with the local resolution displayed below (Left). The local resolution was colored according to the scale displayed. The FSC curves were plotted with Unmasked in blue, Tight in pink, and Corrected in purple (Right). The gold dashed line marks the FSC = 0.143, and the gray dashed line represents FSC = 0.5. The same Class 3 model is docked into (**B**) a yellow Class 2 map and (**C**) a light blue Class 1 map - shown with the corresponding local resolution and FSC curve.

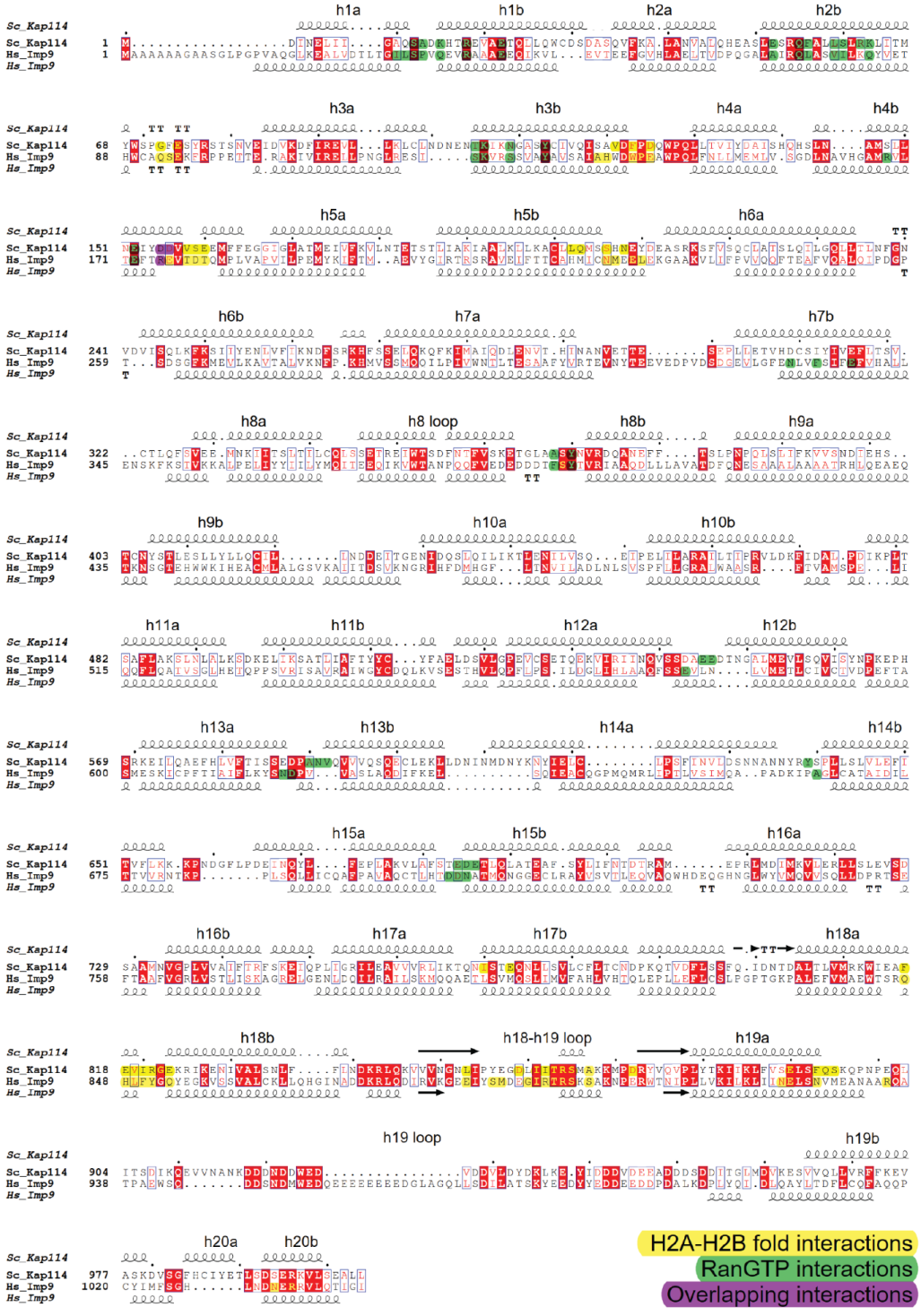

Figure 2 - Supplement 4: Sequence alignment of Kap114 (top) and Imp9 (bottom) was generated using MAFFT. ESPript 3.0 was used to visualize the alignment with the secondary structures annotated from the histone-bound binary structures. The boxed residues in red represent identical residues, and the ones outlined in blue represent similar residues. The HEAT repeats are labeled above Kap114 secondary structure, and contacts in the binary structures are highlighted with H2A-H2B fold/core interactions in yellow, RanGTP interactions in green, and the overlapping interactions by both binary structures in purple.

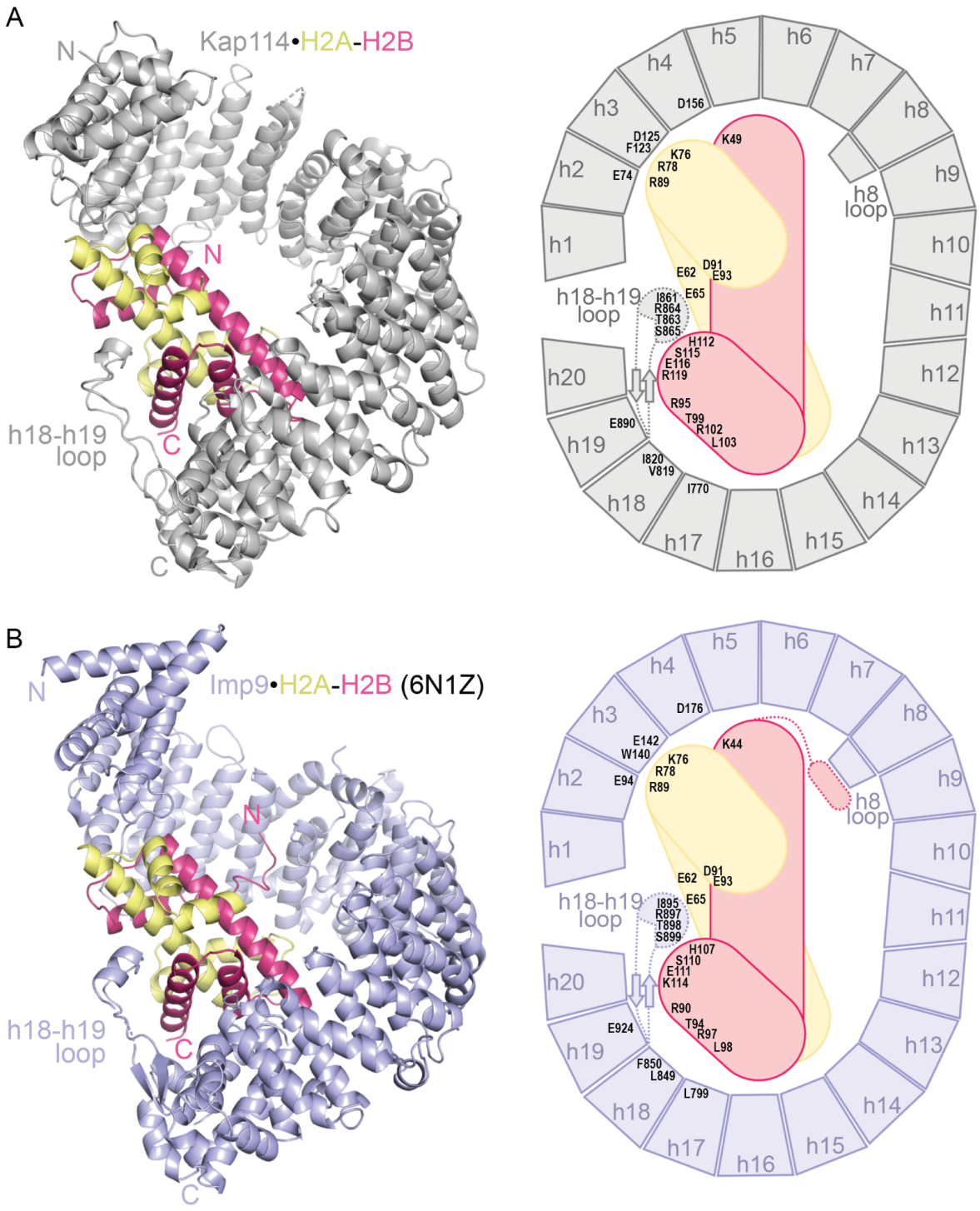

Figure 2 - Supplement 5: (**A**) A cartoon of Kap114•H2A-H2B colored in gray•yellow-red (Left). A schematic with the same color scheme depicts both topology and the conserved residues Imp9 and Kap114 share when contacting H2A-H2B (Right). (**B**) A cartoon of Imp9•H2A-H2B colored in light purple•yellow-red and its schematic.

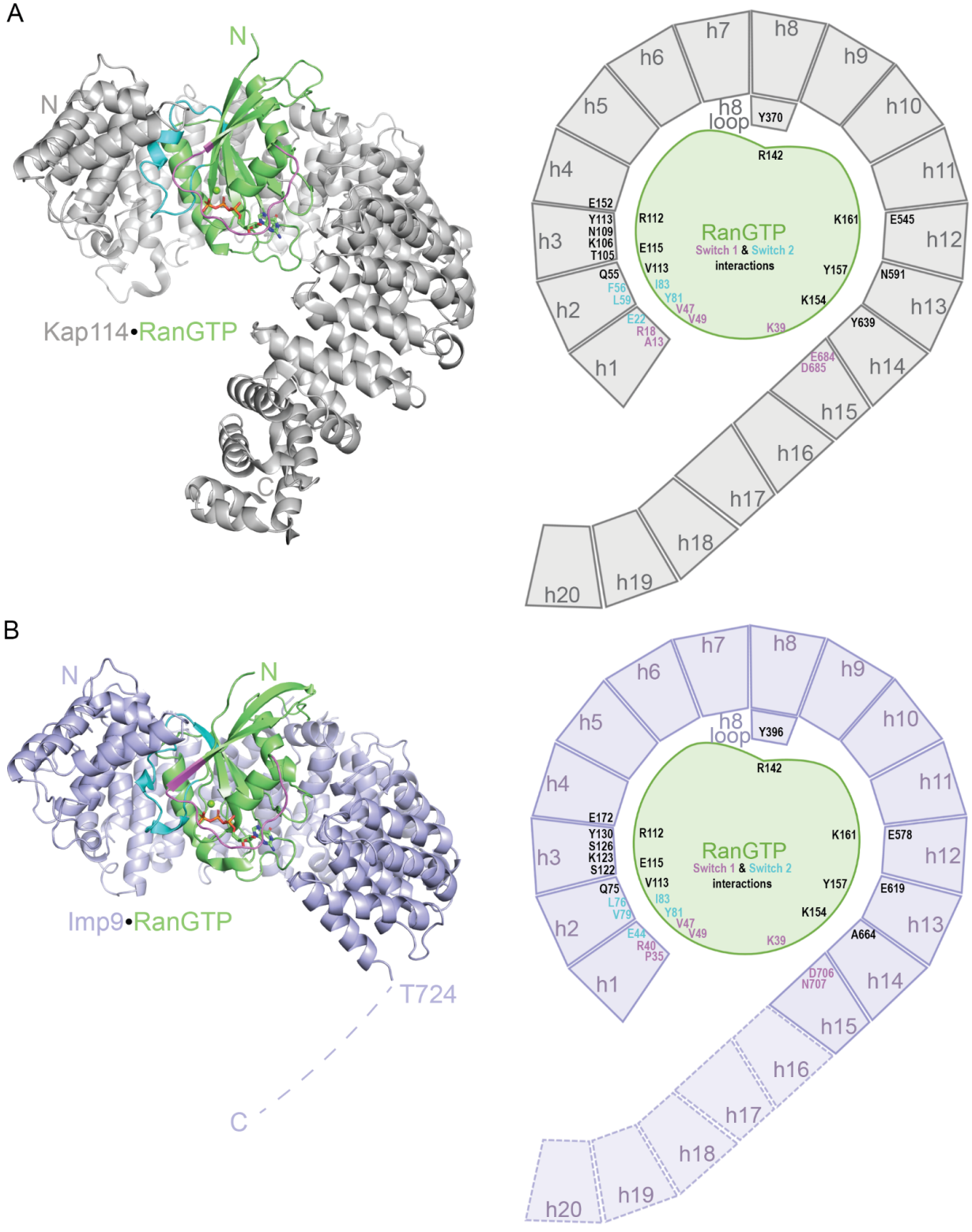

Figure 2 - Supplement 6: (**A**) A cartoon of Kap114•GranGTP colored in gray•green (Left). A schematic with the same color scheme depicts both topology and the conserved residues Imp9 and Kap114 share when contacting RanGTP (Right). (**B**) A cartoon of Imp9•RanGTP colored in light purple•green and its schematic.

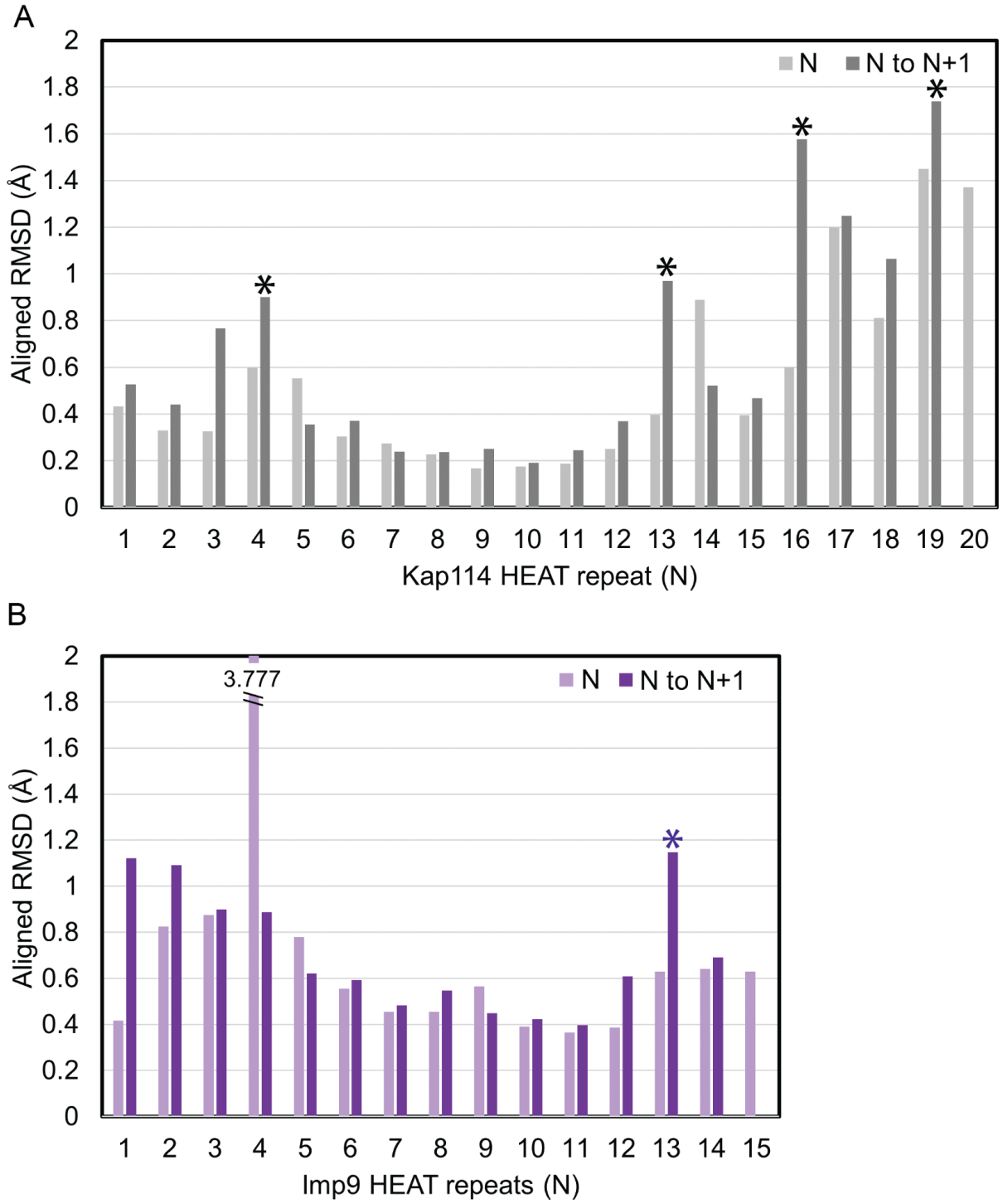

Figure 2 - Supplement 7: The HEAT repeats of the binary Kap114 complexes (A) and binary Imp9 complexes (B) were aligned by individual HEAT repeats, N, and paired HEAT repeats, N to N+1. The asterisk denotes local maximum RMSD between the paired HEAT repeats that corresponds to a hinge.

Figure 2 – Supplement Table 1: Kap114 Cryo-EM data collection, refinement, and validation statistics

	Kap114·H2A-H2B EMD-28788 PDB 8F0X	RanGTP·Kap114 EMD-28782 PDB 8F19	RanGTP·Kap114·H2A-H2B EMD-28796 PDB 8F1E
Data collection and processing			
Facility	PNCC	PNCC	UTSW
Magnification	81kx	81kx	105kx
Voltage (kV)	300	300	300
Electron exposure (e^{-}/Å^2)	50	50	52
Defocus range (μm)	1.5-2.5	1.5-2.5	1.5-2.5
Pixel size (Å)	0.5295	0.5295	0.415
Symmetry imposed	C1	C1	C1
Initial particle images (no.)	6,632,116	7,046,263	3,401,608
Final particle images (no.)	554,529	277,305	134,915
Map resolution (Å)	3.21	3.49	3.28
FSC threshold	0.143	0.143	0.143
Refinement			
Initial model used (PDB code)	6AHO, 6N1Z	6AHO, 3W3Z	8F0X, 8F19
Model resolution (Å)	2.5/3.0/3.3	2.8/3.2/3.6	3.1/3.2/3.5
FSC threshold	0/0.143/0.5	0/0.143/0.5	0/0.143/0.5
Map sharpening *B* factor (Å^2)	158.4	165.0	126.5
Model composition			
Nonhydrogen atom	8,743	8,717	10,174
Protein residues	1,101	1,087	1,273
Ligand	---	2 (GTP; Mg)	2 (GTP; Mg)
B factors (Å^2)			
Protein	58.65	70.40	69.99
Ligand	---	60.23	138.41
R.m.s. deviations			
Bond lengths (Å)	0.004	0.003	0.003
Bond angles (°)	0.647	0.667	0.668
Validation			
MolProbity score	1.40	1.43	1.58
Clashscore	7.37	7.81	11.76
Poor rotamers (%)	0	0	0.17
Ramachandran plot			
Favored (%)	98.36	99.07	98.26
Allowed (%)	1.74	0.93	1.74
Disallowed (%)	0	0	0

Figure 2 – Supplement Table 2: Imp9 Cryo-EM data collection, refinement, and validation statistics

	Imp9·RanGTP EMD-28899 PDB 8F7A
Data collection and processing	
Facility	UTSW
Magnification	105kx
Voltage (kV)	300
Electron exposure (e^{-}/Å^2)	52
Defocus range (μm)	1.5-2.5
Pixel size (Å)	0.417
Symmetry imposed	C1
Initial particle images (no.)	2,198,920
Final particle images (no.)	239,496
Map resolution (Å)	3.78
FSC threshold	0.143
Refinement	
Initial model used (PDB code)	6N1Z, 3W3Z
Model resolution (Å)	3.3/3.5/4.0
FSC threshold	0/0.143/0.5
Map sharpening *B* factor (Å^2)	204.4
Model composition	
Nonhydrogen atom	6,721
Protein residues	849
Ligand	2 (GTP; Mg)
B factors (Å^2)	
Protein	59.02
Ligand	80.04
R.m.s. deviations	
Bond lengths (Å)	0.003
Bond angles (°)	0.611
Validation	
MolProbity score	1.80
Clashscore	10.24
Poor rotamers (%)	0
Ramachandran plot	
Favored (%)	96.06
Allowed (%)	3.82
Disallowed (%)	0.12

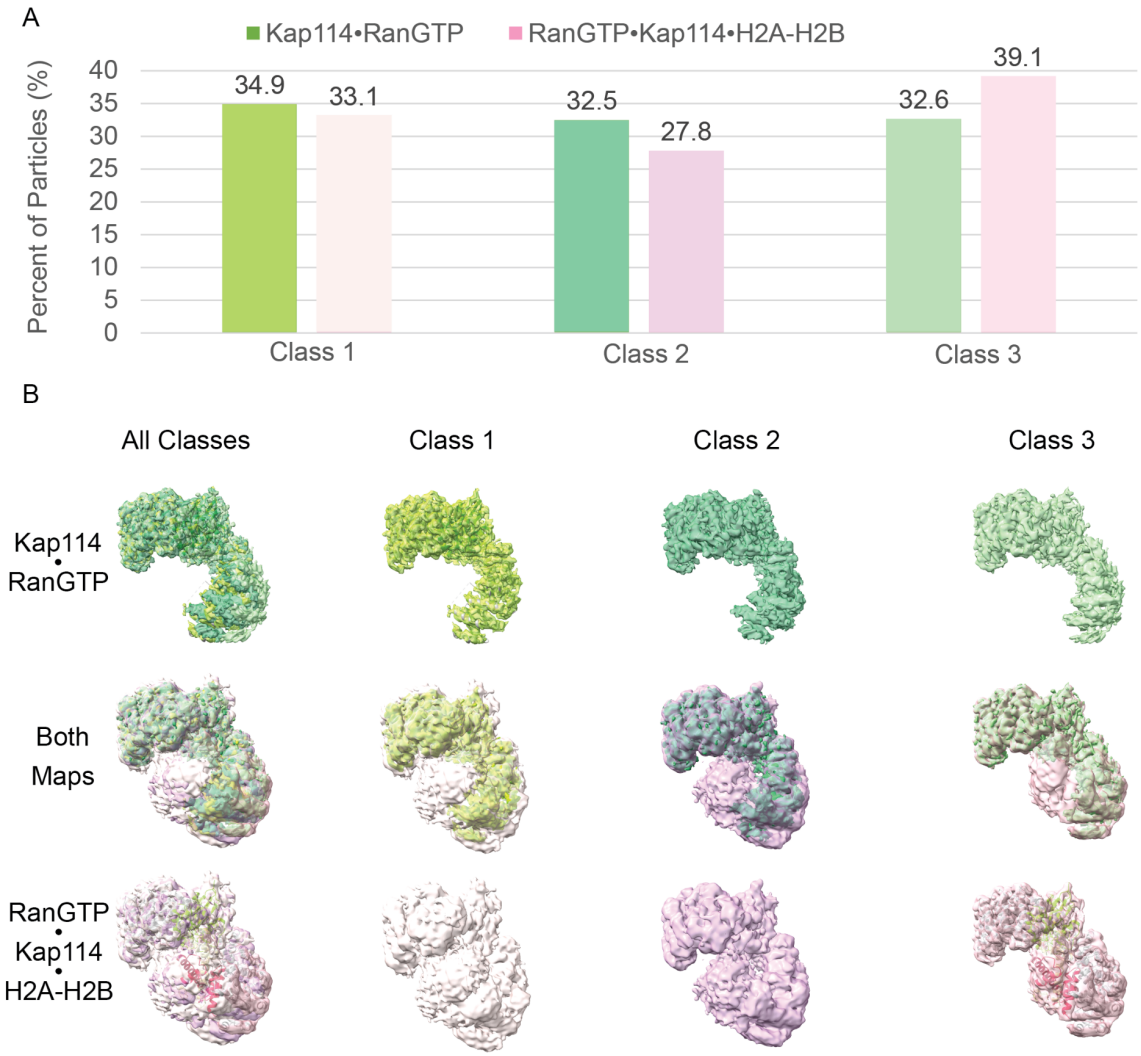

Figure 3 - Supplement 1: Populations of three distinct classes of RanGTP-bound binary and ternary Kap114 complexes. (A) The percentage of particles in each class are plotted in a bar chart with Kap114•RanGTP in green and RanGTP•Kap114•H2A-H2B in pink.(B) A visual overlay of the maps obtained from the three classes for the binary complex in green and the ternary complex in pink. Where Class1 exhibits the smallest degree of opening, Class 3 the widest opening of the three classes, and Class 2 the moderate opening of the Kap C-terminal repeats.

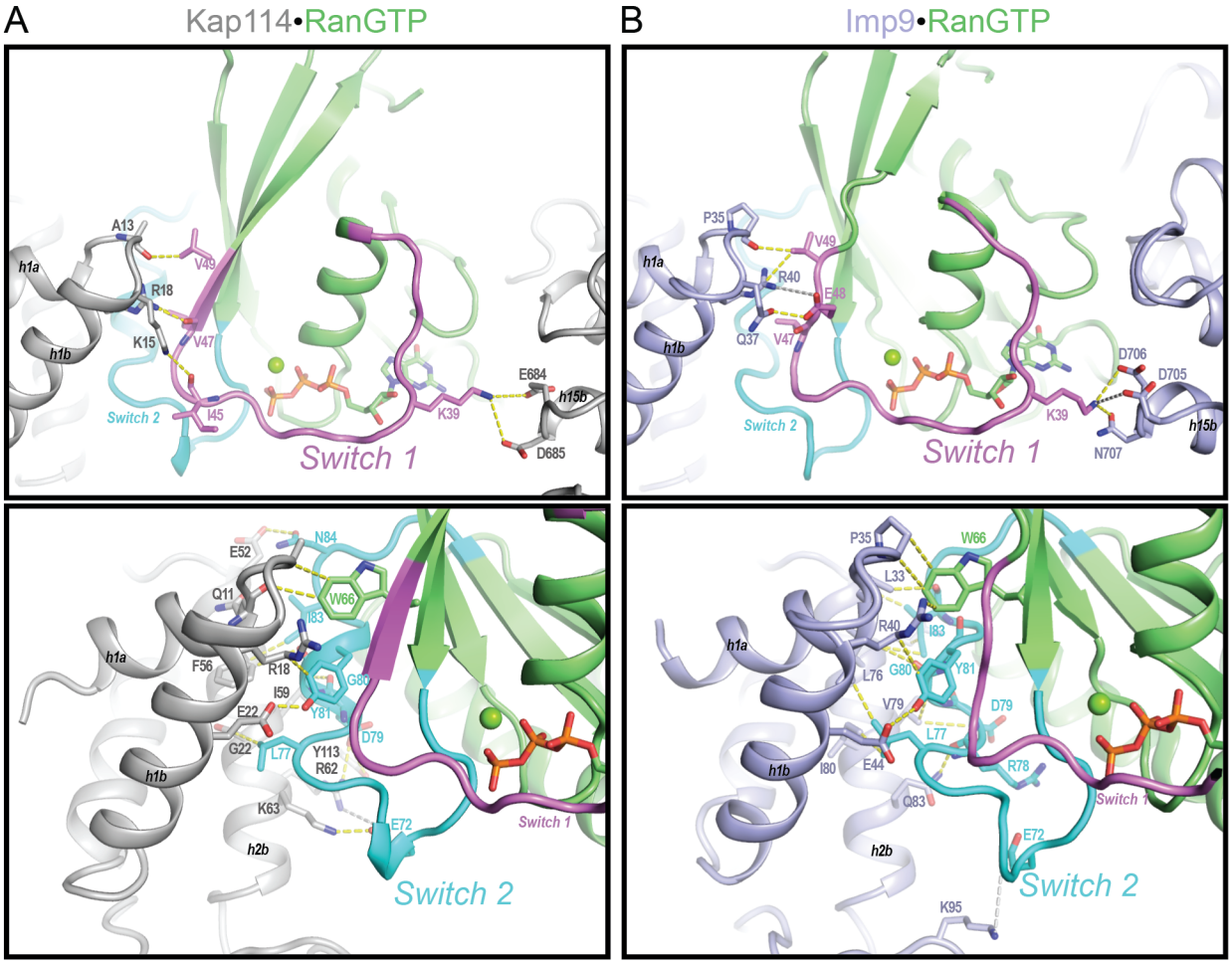

Figure 3 - Supplement 2: Detailed interactions of Kap114•RanGTP (A) and Imp9•RanGTP (B) complex at the switch 1 and switch 2 interface of the RanGTP with Kaps. In all panels, Kap114 is gray, Imp9 is light purple, RanGTP is in green with switch 1 colored violet and switch two colored cyan. The yellow and gray dotted lines represent interactions under <4 Å (yellow) and long-range electrostatic interactions under <8 Å (gray), respectively.

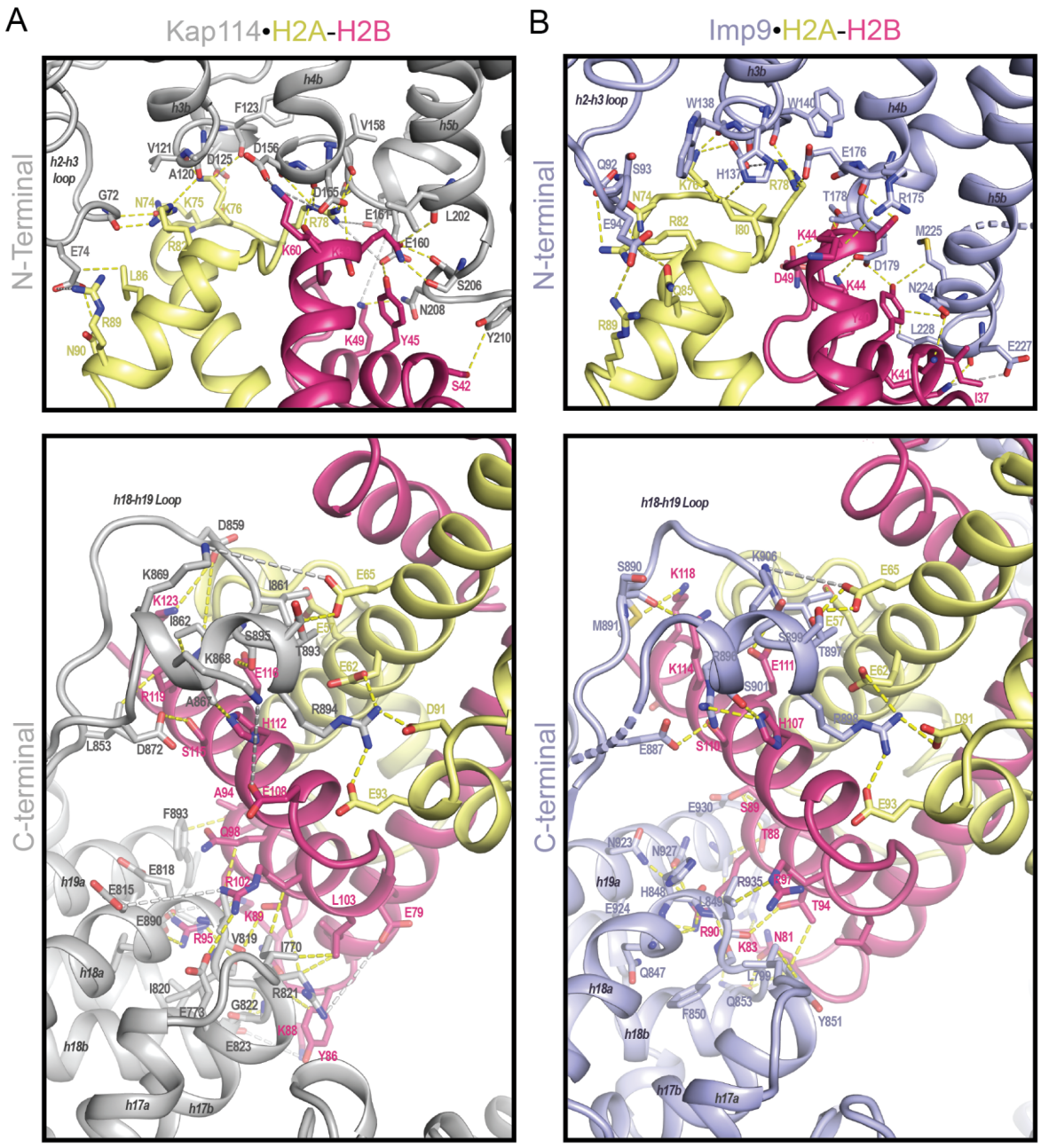

Figure 3 - Supplement 3: Detailed iInteractions of Kap114•H2A-H2B (A) and Imp9•H2A-H2B (B) complex at the NT and CT interface of the Kaps with H2A-H2B. CT of Kap114. In all panels, Kap114 is gray, Imp9 is light purple, H2A is yellow, and H2B is red. The yellow and gray dotted lines represent interactions under <4 Å (yellow) and long-range electrostatic interactions under <8 Å (gray), respectively.

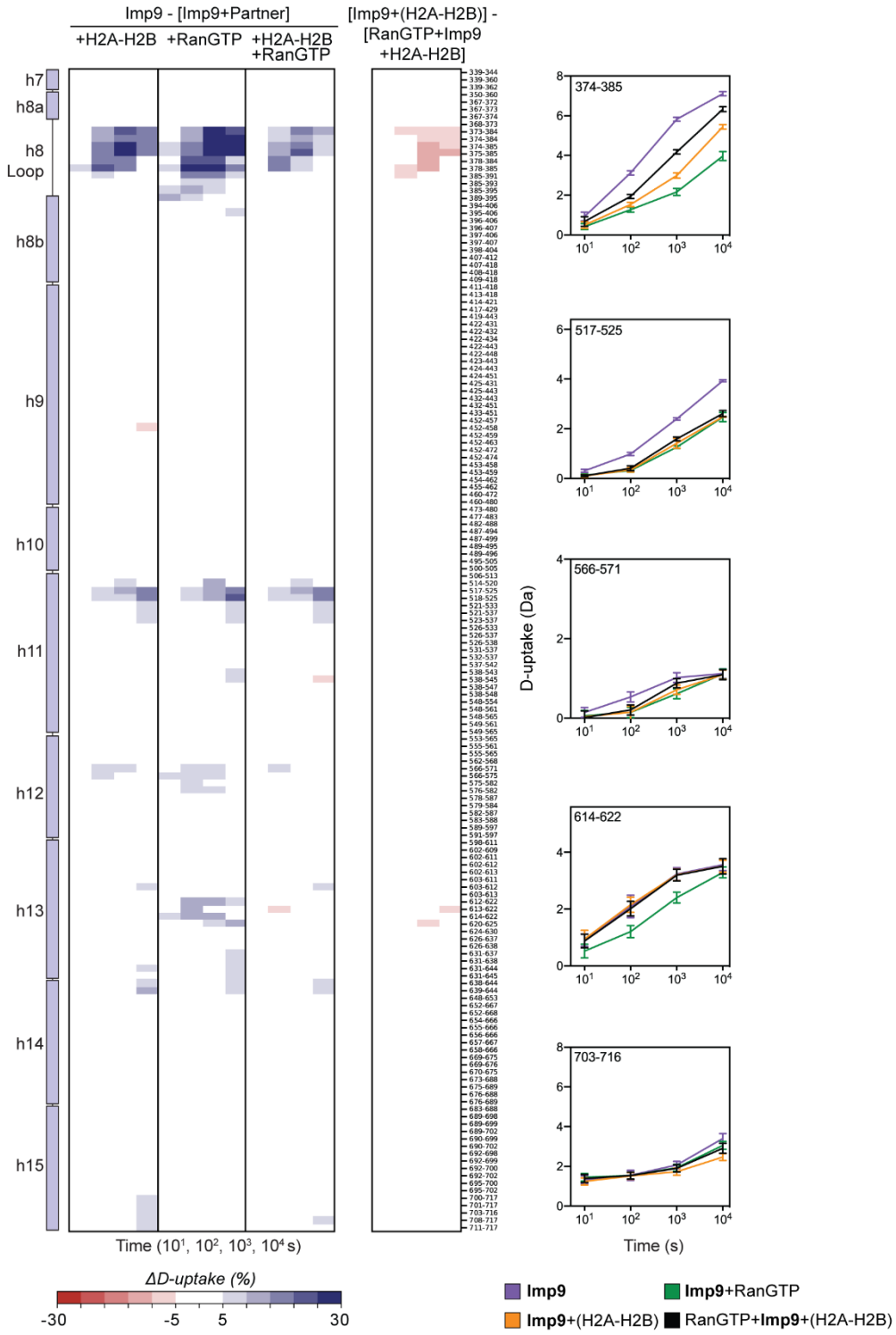

Figure 4 - Supplement 1: Fractional D-uptake differences in Imp9 h7-h15. Differences in D-uptake between Imp9 alone and Imp9+H2A-H2B, Imp9+RanGTP, or RanGTP+Imp9+H2A-H2B in **Panels 1**, **2**, and **3**, respectively. Difference in D-uptake between Imp9+H2A-H2B and RanGTP+Imp9+H2A-H2B is shown in **Panel 4**. Blue/Red coloring indicates a difference ≥5% with a *p*-value ≤0.01 in a Welch's t-test (n=3). D-uptake plots show Imp9 alone (purple), Imp9+H2A-H2B (orange), Imp9+RanGTP (green), and RanGTP+Imp9+H2A-H2B (black). Error bars are ±2SD with n=3. The y-axis is 80% of the maximum theoretical D-uptake, assuming complete back exchange of the N-terminal residue.

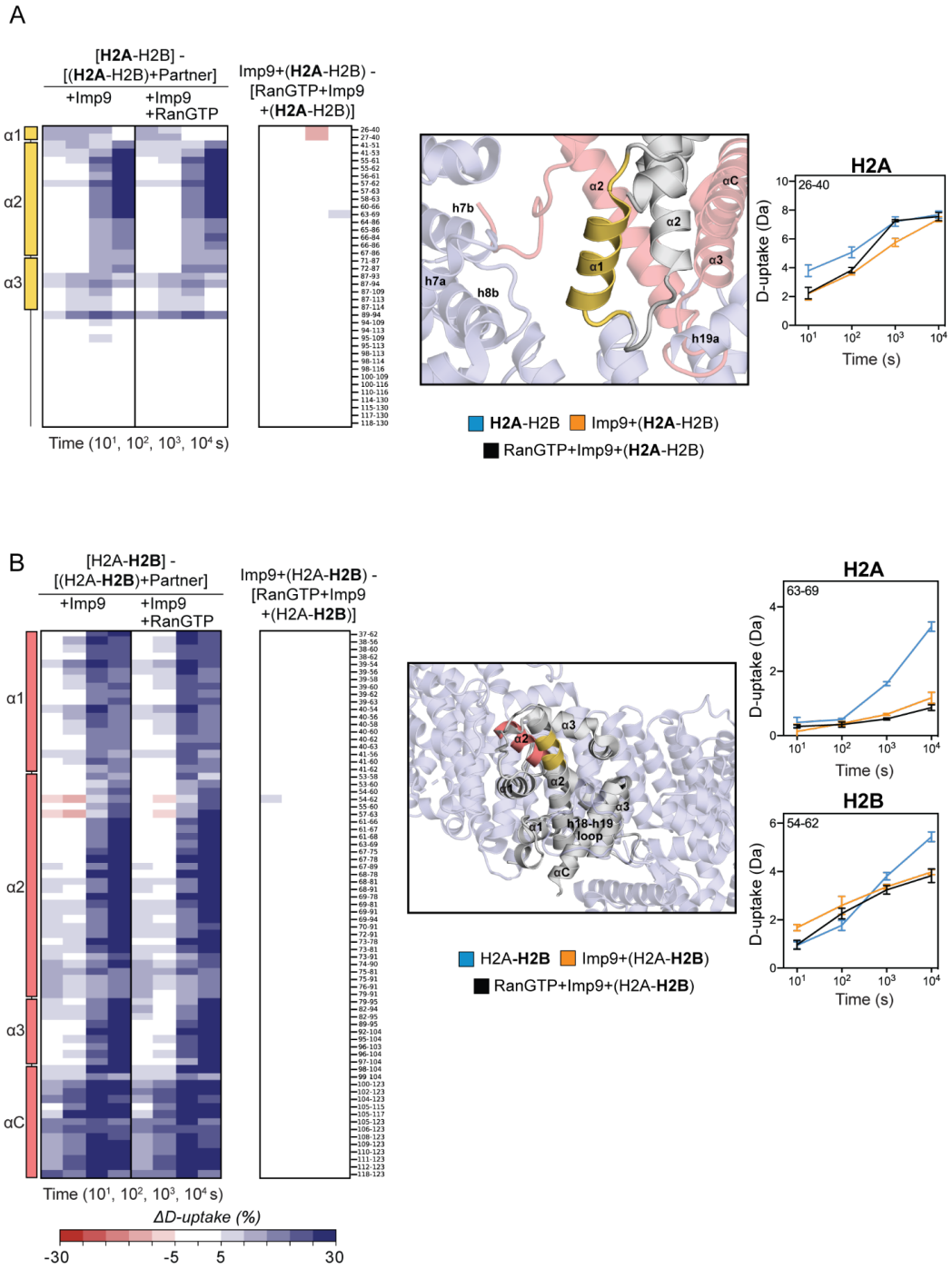

Figure 4 - Supplement 2: Fractional D-uptake differences in H2A and H2B peptides. (**A**) Differences in deuterium uptake between H2A alone and Imp9•H2A-H2B or RanGTP•Imp9•H2A-H2B in **Panel 1**, and **2**, respectively. Difference between Imp9•H2A-H2B and RanGTP•Imp9•H2A-H2B shown in **Panel 3**. H2A changes upon ternary formation with example D-uptake plots for H2A residues 26-40 (colored yellow on structure). (**B**) Differences in deuterium uptake between H2B alone and Imp9•H2A-H2B or RanGTP•Imp9•H2A-H2B in **Panel 1**, and **2**, respectively. Difference between Imp9•H2A-H2B and RanGTP•Imp9•H2A-H2B shown in **Panel 3**. H2A-H2B changes upon ternary formation with example D-uptake plots for H2A residues 63-69 (colored yellow on structure) and H2B 54-62 (colored red on structure). For A and B, Blue/Red coloring indicates a difference ≥5% with a *p*-value ≤0.01 in a Welch's t-test (n=3). D-uptake plots show H2A-H2B alone (blue), Imp9+H2A-H2B (orange), and RanGTP+Imp9+H2A-H2B (black). Error bars are ±2SD with n=3. The y-axis is 80% of the maximum theoretical D-uptake, assuming complete back exchange of the N-terminal residue.

Figure 4 – Supplement Table 3: Summary of HDX data

Samples	Imp9, H2A-H2B, RanGTP, Imp9•H2A-H2B, Imp9•RanGTP, and Imp9•RanGTP•H2A-H2B
Reaction Buffer	20 mM HEPES pH 7.5, 200 mM NaCl, 2 mM $Mg(CH_3COO)_2•4H_2O$, 2 mM TCEP, pH_{read}=7.5
Time Course (s)	10, 10^2, 10^3, 10^4 s at 25°C
Control Samples	Unlabeled Imp9, H2A-H2B, and RanGTP
Replicates (technical)	3
Imp9	
#Peptides	433
Sequence Coverage	94.3%
Average Peptide Length/Redundancy	11.35/5.00
Global Significance Threshold	ΔHDX=0.29 Da or 2.9%*
Mean Back-exchange (% possible D-uptake)	43.1%
H2A	
#Peptides	39
Sequence Coverage	80.0%
Average Peptide Length/Redundancy	14.36/5.38
Global Significance Threshold	ΔHDX=0.43 Da or 3.2%*
Mean Back-exchange (% possible D-uptake)	34.0%
H2B	
#Peptides	73
Sequence Coverage	69.0%
Average Peptide Length/Redundancy	14.96/12.55
Global Significance Threshold	ΔHDX=0.43 Da or 3.48%*
Mean Back-exchange (% possible D-uptake)	36.4%
RanGTP	
#Peptides	89
Sequence Coverage	96.2%
Average Peptide Length/Redundancy	12.42/5.53
Global Significance Threshold	ΔHDX=0.31 Da/2.88%
Mean Back-exchange (% possible D-uptake)	47.0%

*Calculated as the propagated standard error of the mean. Implemented significance threshold of ≥5% with a *p*-value ≤0.01 in a Welch's t-test (n=3)

Figure 4 – Supplement Table 4-6: HDX state data for Imp9, H2A-H2B, and RanGTP (Attached as .csv)

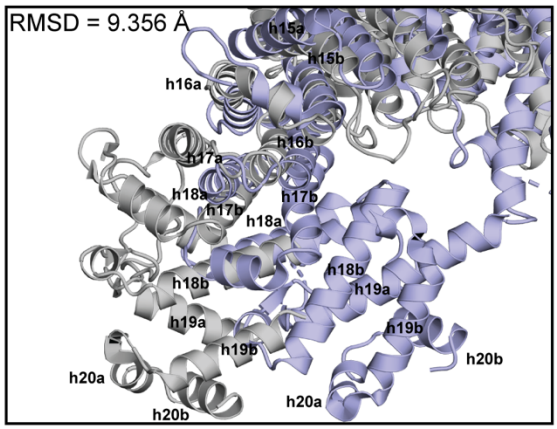

RanGTP•Kap114•(H2A-H2B)
Imp9•(H2A-H2B)

Figure 6 - Supplement 1: Superposition of Imp9•H2A-H2B and RanGTP•Kap114•H2A-H2B (RMSD=9.356 Å). RanGTP and H2A-H2B are hidden, while Kap114 (gray) and Imp9 (light blue) are shown. h15-h20 a and b helices are labeled for clarity. h16-h17 is the hinge on which the rest of the C-terminal repeats move (742-805 of Imp9 and 713-776 of Kap114).

Figure 7 – Supplement Table 7: HDX-based Prediction of the Affinity of RanGTP for Imp9 in the Ternary Complex

Region	Peptides	Average ΔHDX±SD Loss in Ternary Complex (%)*	Predicted K_D (nM)**
Imp9 residues 38-52 that bind RanGTP	38-45 38-46 39-46 42-51 46-51 46-52 47-52	45.3±10.8 [indicating only 54.7% of RanGTP bound to Imp9 in the ternary complex compared to 100% bound in the binary complex]	~200 nM

*Calculated as $(1 - \frac{\text{Imp9}-\text{Imp9}_{Ternary}}{\text{Imp9}-\text{Imp9}_{Binary}})$ x 100%, where $\text{Imp9}_{\text{Binary}}$ is Imp9•RanGTP at 10^4 s.

**Estimated using spreadsheet from Kochert et al. 2018.

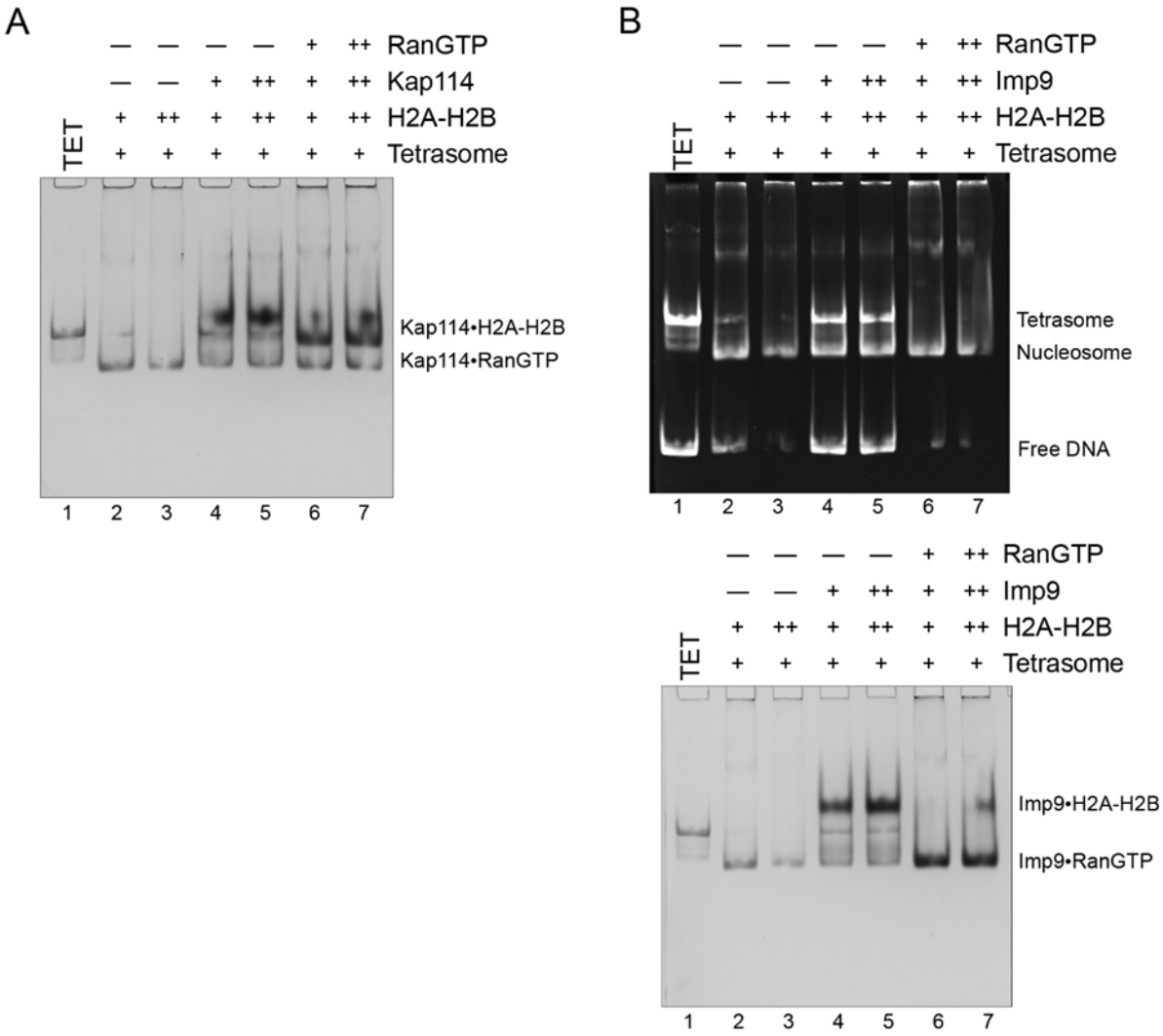

Figure 8 - Supplement 1: Nucleosome assembly assays. (**A**) Nucleosome assembly assay where either H2A-H2B, Kap114•H2A-H2B or RanGTP•Kap114•H2A-H2B is titrated in molar equivalents of 2.0 and 3.0 to tetrasome (TET; 1.25 μM). Native page gel was Coomassie-stained. Ethidium bromide-stained gel is in ***Figure 8A***. (**B**) Nucleosome assembly assay where either H2A-H2B, Imp9•H2A-H2B or RanGTP•Imp9•H2A-H2B is titrated in molar equivalents of 2.0 and 3.0 to tetrasome (TET; 1.25 μM). Images of the same native gel, ethidium bromide-stained (top) and Coomassie-stained (bottom) are aligned for comparison. Source data for A-B is in ***Figure 8 – Supplement 1 - Source Data 1-2*** respectively.

Source Data Legends

Figure 1 - Source Data 1: Pull-down binding assay of MBP-Kap114 immobilized on amylose beads with H2A-H2B and RanGTP. After extensive washing, bound proteins were visualized by Coomassie-stained SDS-PAGE.

Figure 1 - Source Data 2: Constant Kap114 (lanes 2-7) was titrated with 0.5, 1, or 1.5 molar ratio of RanGTP (lanes 2-4) or H2A-H2B (lane 5-7). Constant Kap114•H2A-H2B was titrated with 0.5, 1, or 1.5 molar ratio of RanGTP (lanes 8-10). Protein was visualized by Coomassie-stained native PAGE.

Figure 1 - Source Data 3: DNA competition assay with Kap114 (lanes 4-6) titrated at 0.5, 1, or 1.5 molar equivalents of H2A-H2B (in a DNA•H2A-H2B 1:7 complex), while Kap114•RanGTP (1:1, lanes 8-10) is titrated at 0.25, 0.5, or 1.0 molar equivalents of H2A-H2B (in a DNA•H2A-H2B 1:7 complex). Native PAGE was visualized with ethidium bromide.

Figure 1 - Supplement 1 - Source Data 1: Pull-down binding assays of immobilized MBP on amylose beads with untagged Kap114, H2A-H2B, and RanGTP added. After extensive washing, bound and input proteins were visualized by Coomassie-stained SDS-PAGE.

Figure 1 - Supplement 1 - Source Data 2: Constant Imp9 (lanes 2-7) was titrated with 0.5, 1, or 1.5 molar ratio of RanGTP (lanes 2-4) or H2A-H2B (lane 5-7). Constant Imp9•H2A-H2B was titrated with 0.5, 1, or 1.5 molar ratio of RanGTP (lanes 8-10). Protein was visualized by Coomassie-stained native PAGE.

Figure 1 - Supplement 1 - Source Data 3: DNA competition assay with Kap114 (lanes 4-6) titrated at 0.5, 1, or 1.5 molar equivalents of H2A-H2B (in a DNA•H2A-H2B 1:7 complex), while Kap114•RanGTP (1:1, lanes 8-10) is titrated at 0.25, 0.5, or 1.0 molar equivalents of H2A-H2B (in a DNA•H2A-H2B 1:7 complex. Native PAGE was visualized with Coomassie staining.

Figure 1 - Supplement 1 - Source Data 4: DNA competition assay with Imp9 (lanes 4-6) titrated at 0.5, 1, or 1.5 molar equivalents of H2A-H2B (in a DNA•H2A-H2B 1:7 complex), while Imp9•RanGTP (1:1, lanes 8-10) is titrated at 0.25, 0.5, or 1.0 molar equivalents of H2A-H2B (in a DNA•H2A-H2B 1:7 complex. Images of the same native gel, ethidium bromide-stained and Coomassie-stained, are included.

Figure 8 - Source Data 1: Nucleosome assembly assay where either H2A-H2B, Kap114•H2A-H2B or RanGTP•Kap114•H2A-H2B is titrated in molar equivalents of 2.0 and 3.0 to tetrasome (TET; 1.25 μM). Ethidium bromide-stained gel is shown.

Figure 8 - Supplement 1 - Source Data 1: Nucleosome assembly assay where either H2A-H2B, Kap114•H2A-H2B or RanGTP•Kap114•H2A-H2B is titrated in molar equivalents of 2.0 and 3.0 to tetrasome (TET; 1.25 μM). Native page gel was Coomassie-stained.

Figure 8 - Supplement 1 - Source Data 2: Nucleosome assembly assay where either H2A-H2B, Imp9•H2A-H2B or RanGTP•Imp9•H2A-H2B is titrated in molar equivalents of 2.0 and 3.0 to tetrasome (TET; 1.25 μM). Images of the same native gel, ethidium bromide-stained and Coomassie-stained, are included.